High-resolution luminescence-dated sediment record for the last two glacial-interglacial cycles from Rodderberg, Germany

Junjie Zhang[1*], Bernd Zolitschka[2], Ines Hogrefe[2], Sumiko Tsukamoto [1], Franz Binot [1], Manfred Frechen[1]

[1] Leibniz Institute for Applied Geophysics, Stilleweg 2, 30655 Hannover, Germany

[2] Institute of Geography, University of Bremen, Celsiusstrasse 2, 28359 Bremen, Germany

*Corresponding author: Junjie.Zhang@leibniz-liag.de

High-resolution luminescence-dated sediment record for the last two glacial-interglacial cycles from Rodderberg, Germany

Junjie Zhang[1*], Bernd Zolitschka[2], Ines Hogrefe[2], Sumiko Tsukamoto [1], Franz Binot [1], Manfred Frechen[1]

[1] Leibniz Institute for Applied Geophysics, Stilleweg 2, 30655 Hannover, Germany

[2] Institute of Geography, University of Bremen, Celsiusstrasse 2, 28359 Bremen, Germany

*Corresponding author: Junjie.Zhang@leibniz-liag.de

Abstract

The Rodderberg Volcanic Complex (RVC) is well-known for the long and probably continuous climate record archived in its crater basin, which lasts for several glacial-interglacial cycles. However, a detailed chronological framework is still lacking. Here, we perform high-resolution luminescence dating on a 72.8 m-long sediment core with the optically stimulated luminescence (OSL) signal from fine-grained (4–11 µm) quartz and three kinds of post-infrared infrared (pIRIR) stimulated luminescence signals from fine-grained polymineral fractions. Quartz OSL ages align well with pIRIR ages for the last 50 ka, but they underestimate in relation to pIRIR ages for ages beyond 50 ka. The three pIRIR signals, including the pIRIR signal at 225 °C ($pIRIR_{225}$), the pulsed pIRIR signal at 150 °C (pulsed $pIRIR_{150}$) and the multi-elevated-temperature pIRIR at 250 °C (MET-$pIRIR_{250}$), yield consistent ages up to ca. 250 ka at a sediment depth of 37.5 m. Below that depth, dating limits of the protocols are exceeded. Nevertheless, our results indicate that sediments below 37.5 m predate Marine Isotope Stage (MIS) 7. Altogether, obtained ages reveal continuous dust accumulation during MIS 7 and MIS 6. One erosional event happened at the end of the Eemian (MIS 5e), which eroded the Eemian soil. The sedimentation rate during the Weichselian glacial period is tenfold lower compared to the sedimentation rate observed during MIS 7–6. This low sedimentation rate likely arises from the cessation of slope-wash effects and the occurrence of various erosional events alternating with dust deposition. A notably high sedimentation rate is observed at the transition from MIS 6 to Eemian, marked by the deposition of a 6 m-thick loess layer between 132 and 129 ka. This high sedimentation rate could be attributed to intensified slope-wash and solifluction processes resulting from the thawing of permafrost. Alternatively, it might be a signature of an abrupt cold pulse such as Heinrich event 11.

Keywords: Rodderberg, crater sediments, OSL dating, pIRIR, two glacial-interglacial cycles

1. Introduction

Prediction of future climate change relies on our knowledge of past climate change. In this regard, climate archives such as polar ice cores and deep-sea sediments provide long-term information about global climate change (Lorius et al., 1990; Lisiecki and Raymo, 2005). In addition, loess deposits provide proxies of terrestrial climate change on regional to continental scales. In certain regions such as the Chinese Loess Plateau, loess deposits cover a large area and also span long periods with many glacial/interglacial cycles (Liu and Ding, 1998; Maher, 2016). However, loess deposits in Europe are relatively patchy in distribution and frequently incomplete due to erosional events (Boenigk and Frechen, 2001; Frechen et al., 2003; Lehmkuhl et al., 2016; Zens et al., 2018). Large gaps, reaching up to 100 ka, have been identified through luminescence dating for several of these loess sections (Schmidt et al., 2011b, 2014; Kreutzer et al., 2012; Thiel et al., 2014; Steup and Fuchs, 2017). This lack of long-term and continuous climate archives hampers our understanding of palaeoclimatic change in Europe.

The Eifel volcanic region in western Germany is characterized of numerous scoria cones (Schmincke et al., 2007; Sirocko et al., 2016). These volcanic formations serve as highly effective sediment traps. In the West Eifel Volcanic Field, dozens of extant and dry maar lakes provide high-resolution climate records with laminated sediments (Negendank et al., 1990; Zolitschka et al, 2000; Sirocko et al., 2005, 2016; Seelos et al., 2009; Römer et al., 2016). However, these often annually laminated sediments only encompass the most recent glacial-interglacial cycle. In the east Eifel region, long-term deposits of loess and loess derived sediments that extend beyond the last interglacial are preserved in several crater basins (Boenigk and Frechen, 2001; Schmidt et al., 2014). Especially, the Rodderberg Volcanic Complex (RVC), located south of Bonn and close to Rhine River, is a good candidate to provide climatic records over several glacial-interglacial cycles. According to previous studies, the bowl-shaped Rodderberg crater served as a sediment trap accumulating aeolian dust, lake sediments and tephra since more than 300 ka (Zolitschka et al., 2014 and references therein).

Despite the potential of this sediment trap for palaeoclimate reconstruction, its temporal framework is not well constructed. Pioneering studies attempting to constrain the eruption age of the Rodderberg volcano rely on the stratigraphic context. Remy (1960) suggested an eruption age of 30 ka as the Rodderberg tephra was intercalated with Weichselian loess units in the surroundings of Rodderberg, while Bartels and Hard (1973, 1974) proposed an eruption age of 370–250 ka based on the observation that the Rodderberg tephra was located below at least two palaeosol horizons west of the Lannesdorf town. Bibus (1980) reported tuff and scoria rings lying above a fluvial terrace of the Rhine River, while the terrace has an assumed age of ca. 500 ka. Later, Boenigk and Frechen (2006) suggested that this age estimate of 500 ka is the maximum

age for the onset of Rodderberg volcanism. Over the last two decades, thermoluminescence (TL) dating has been utilized as an absolute dating technique to determine the eruption age of the Rodderberg volcano. TL ages of one siltstone xenolith and two phreatomagmatic tuff samples from the RVC have been reported (Blanchard, 2002; Paulick et al., 2009; Zöller and Blanchard, 2009). The siltstone xenolith had an age of 321±37 ka without fading correction and the two tuff samples generated ages of 300±97 ka and 334±59 ka after short-term fading corrections (Paulick et al., 2009; Zöller and Blanchard, 2009). Anomalous fading is the loss of the luminescence signal under ambient temperature (Wintle, 1973). If not properly corrected, it results in age underestimation. Thus, all of these studies emphasized that their TL ages should be treated as minimum ages. Therefore, volcanic eruptions certainly ended prior to 300 ka (Blanchard, 2002; Paulick et al., 2009; Zöller and Blanchard, 2009).

Several drilling activities have been carried out at Rodderberg to retrieve its crater infill. Detailed information about the drilled cores has been summarized by Zolitschka et al. (2014). Among them, one drilling operated in the year 2000 (Klostermann et al., 2000) yielded a 55 m-long record (core KB1) with the upper 40 m consisting of loess and the lower 15 m of lacustrine sediments (Zöller et al., 2010). Blanchard (2002) dated one sediment sample from 50 m depth of KB1 with both TL and infrared-stimulated luminescence (IRSL) dating methods but without fading correction. Obtained TL and IRSL ages were 107±27 ka and 66±13 ka, respectively (Blanchard, 2002; Paulick et al., 2009; Zöller et al., 2010). The discrepancy between TL and IRSL ages has been attributed to the incomplete resetting of the TL signal and/or the higher fading rate of the IRSL signal (Zöller et al., 2010). Following the study of Blanchard (2002), Fischer (2004) applied TL and IRSL dating on several sediment samples from depths between 4 and 50 m of KB1. However, all of the tested samples displayed saturation in their natural TL and IRSL signals and no ages were reported (Fischer, 2004; Zöller et al., 2010). Furthermore, the blue-stimulated OSL signal of quartz was tested on a sample from 30.1 m depth and it was also saturated (Fischer, 2004; Zöller et al., 2010).

A new drilling project was performed from 2011 to 2012 adjacent to KB1 with three holes cored in the centre of the crater recovering the 72.8 m-long sediment sequence ROD11 down to volcanic rocks (Zolitschka et al., 2014). Based on lithological changes and preliminary pollen data, Zolitschka et al. (2014) suggested that three interglacials were preserved in this core. A comprehensive analysis of pollen conducted by Schläfli et al. (2023) concentrated on the lowermost Rodderberg interglacial (LRI). This study revealed a remarkable similarity between the pollen assemblage of LRI and that of the Kärlich interglacial (Bittmann, 1992), suggesting that the LRI most likely corresponds to Marine Isotope Stage (MIS) 11. Hitherto, no absolute dating has been performed for ROD11 and prior attempts to apply TL and IRSL dating on core

KB1 failed to produce dependable ages (Blanchard, 2002; Fischer, 2004; Zöller et al., 2010). Thus, a robust chronological framework for ROD11 is needed for palaeoclimatic interpretations.

Earlier IRSL dating studies mainly performed the IR stimulation at 50 °C. Thomsen et al. (2008) reported that the post-infrared IRSL signal (post-IR IRSL or pIRIR) of feldspar stimulated at an elevated temperature (e.g., at 225 °C, $pIRIR_{225}$) after a prior IR stimulation at 50 °C (IR_{50}) exhibits much lower fading rates. Thus, the two-step IR stimulation protocol was proposed for dating (Buylaert et al., 2009). Fading correction is still needed for the $pIRIR_{225}$ signal. However, with a smaller fading rate the age uncertainty brought in by fading correction would be smaller (Buylaert et al., 2009). Following studies modified this $pIRIR_{225}$ dating protocol in order to get a non-fading pIRIR signal, such as the $pIRIR_{290}$ protocol (Thiel et al., 2011), the pulsed $pIRIR_{150}$ protocol (Schmidt et al., 2011a) and the multiple-elevated-temperature (MET) $pIRIR_{250}$ protocol (Li and Li, 2011).

In this study, we aim at generating a reliable temporal framework for the sediment sequence of ROD11 by applying various pIRIR dating protocols on fine-grained (4–11 µm) polymineral samples with high spatial resolution. The ages generated by different pIRIR protocols are then compared with each other to check their reliability. OSL dating of quartz has also been performed for samples from the upper part of ROD11. Finally, a Bacon age-depth model will be generated for the sediment sequence of ROD11 allowing for a much improved palaeoclimatic interpretation.

2. Materials and methods

2.1 Materials

Three holes (ROD11-1, ROD11-2, ROD11-3) were drilled from September 2011 to January 2012 in the centre of the Rodderberg crater (Fig. 1). The three holes are located less than 20 m from each other (50°38’42” N, 7°11’32” E, 147.2 m a.s.l.). More details are presented by Zolitschka et al. (2014). Core ROD11-1 is 164 m deep and was carried out with a rotary drill. Core cuttings with a spatial resolution of 3 m formed the base of the pilot study (Zolitschka et al., 2014) presenting the lithology and preliminary physical and chemical characteristics as well as few pollen data. Cores ROD11-2 and ROD11-3 were combined to generate the composite sediment sequence ROD11 with a maximum composite depth of 72.8 m, below which are volcaniclastic and volcanic rocks (Zolitschka et al., 2014). Samples used in this study were taken from both ROD11-2 and ROD11-3 with depths always provided as composite depths. From the lithological investigation, the sediments of ROD11 have two depositional phases. Below 17 m depth, the

sediments are layered deposits implying a lake or at least moist condition (swamp) in the crater centre with lake sediments and loess derivates. Above 17 m, it changes to dry (aeolian) deposition with loess.

2.2 Luminescence dating

Luminescence dating is being widely applied to date the burial events of Quaternary sediments (Murray et al., 2021). Quartz and feldspar are the most popular minerals used for luminescence dating. A fundamental requirement is that the mineral grains are adequately exposed to sunlight prior to burial allowing the luminescence signal to be reset to zero. Following burial, as the mineral grains are exposed to irradiation from their surrounding environment, electrons from the valence band of the crystal lattice are evicted and accumulate in electron traps which are responsible for the luminescence signal. The equivalent dose (D_e), which represents the total irradiation dose received during the burial, is estimated by measuring the natural luminescence intensity, while the environmental dose rate ($\dot{D}$) is deduced from the concentration of radioactive nuclides (U, Th, K) of the sediments. Luminescence ages are calculated by the equation: Age = $D_e/\dot{D}$.

The quartz OSL signal is bleached much faster compared to the feldspar IRSL signal and it exhibits no fading, which are advantages for luminescence dating. However, the quartz OSL signal saturates at relatively low doses. Previous studies show that D_e measurements of quartz are usually not reliable when the D_e is beyond 150–200 Gy, corresponding to an age of ca. 40–50 ka (Buylaert et al., 2007; Timar-Gabor et al., 2017; Perić et al., 2019). Compared to the quartz OSL signal, the IRSL signal from feldspar reaches saturation at higher doses, which enables dating for older samples. In this study, we apply quartz OSL dating for young samples (<50 ka) and three different pIRIR protocols to date all other samples: the $pIRIR_{225}$ protocol (Buylaert et al., 2009), the pulsed $pIRIR_{150}$ protocol (Schmidt et al., 2011a), and the MET-$pIRIR_{250}$ protocol (Li and Li, 2011).

2.2.1 Sample preparation, measurement facilities and dose rate estimation

Sampling of the core and preparation of samples were performed under subdued red light. The surface of each sample was scraped off by a knife to avoid the effect of light exposure. Inner parts of the samples were reacted with $Na_2C_2O_4$, 10% HCl and 30% H_2O_2 solutions to destroy aggregates and remove carbonates as well as organic matter, respectively. Afterwards, the 4–11 μm grain size fraction (polymineral fine grains) was separated following Stokes law. For some samples, part of the polymineral fraction was further reacted with 30% silica-saturated hydrofluorosilicic acid (H_2SiF_6) to obtain a pure quartz fraction. For measurement of the luminescence signal, 2 mg of polymineral or quartz grains were deposited from suspension in water onto aluminum discs.

Luminescence measurements were carried out on a Risø-TL/OSL DA-15 reader. The built-in $^{90}Sr/^{90}Y$ beta source has a dose rate of 0.07 Gy/s for fine grains (4–11 µm) on aluminum discs. Aliquots of fine-grained quartz were stimulated by blue LEDs (470 nm; 90% of maximum power of 40 mW cm^{-2}), and the OSL signal was detected through a 7.5 mm thick U-340 filter (transmission band in the wavelength of ultraviolet light). Aliquots of fine-grained polymineral were stimulated by IR LEDs (870 nm; 90% of maximum power of 125 mW cm^{-2}) and the IRSL signal was detected through a combined filter package of Schott BG-39 and Corning 7-59 (transmission band of 320–480 nm). The IRSL signal of the polymineral originates from feldspar.

To calculate the environmental dose rates, U, Th and K concentrations of the samples were measured with gamma spectrometry. Water contents were measured by drying in an oven at 110 °C. Samples were stored for one month before gamma spectrometry measurements to reach ^{222}Rn equilibrium. The conversion factors from Liritzis et al. (2013) were used for dose rate calculation. Cosmic ray dose-rates were estimated following Prescott and Hutton (1994). An alpha efficiency (*a*-value) of 0.09 ± 0.02 was used for polymineral pIRIR signals (Kreutzer et al., 2014; Schmidt et al., 2018) and an *a*-value of 0.04 ± 0.01 was used for the quartz OSL signal (Rees-Jones and Tite, 1997). Alpha attenuation factors of 0.84 and 0.86 were adopted for U and Th series, respectively, based on a median grain size of 7.5 µm for the fine grains (Brennan et al., 1991). The mean activity ratio of ^{210}Pb to (^{214}Pb+^{214}Bi), i.e. the average activity of ^{214}Pb and ^{214}Bi, is 1.00 ± 0.07 for all samples below 0.5 m depth (Fig. 2), thus no ^{222}Rn loss is assumed (De Corte et al., 2006). For the sample at 0.5 m depth (LUM4606), the activity ratio of ^{210}Pb to (^{214}Pb+^{214}Bi) was 0.75, and 25% ^{222}Rn loss was applied for its dose rate calculation.

2.2.2 Quartz OSL dating

The single-aliquot regenerative-dose (SAR) protocol (Wintle and Murray, 2006) was used for quartz OSL dating (Table 1). An extra cycle with IR stimulation before OSL stimulation was added. The ratio of the OSL signal after IR stimulation to the OSL signal without IR stimulation – the IR depletion ratio – was used to detect any feldspar contamination (Duller, 2003). An IR depletion ratio close to 1 indicates no feldspar contamination. OSL was measured at 125 °C for 40 s. Early background subtraction was used for D_e estimation with the initial 0–0.48 s signal subtracting the following 0.49–1.60 s signal. The dose-response curve and OSL decay curves for one aliquot of LUM4607 are shown on Fig. 3. The suitable preheat temperature was determined by the D_e vs. preheat temperature test with the sample LUM4371. Preheat temperature was raised from 160 to 300 °C with an interval of 20 °C. Cutheat temperature was always 20 °C lower than the preheat temperature.

Dose recovery tests were performed on several samples. Aliquots were bleached by blue LEDs for 100 s at room temperature two times with a pause of 10,000 s in between. Laboratory doses, which are close to the samples' D_e values, were administered to the bleached aliquots and then measured with the SAR protocol with 220 °C preheat and 200 °C cutheat. The dose recovery ratio (DRR) was calculated by dividing the recovered dose by the given dose. A DRR within the range of 1.0±0.1 is regarded as a successful dose recovery.

To check the thermal stability of quartz OSL signals, isothermal annealing experiments were performed on samples LUM4608 and LUM4632 to estimate the lifetimes of OSL signals. Two aliquots were tested for each sample. A regenerative dose of 60 Gy and a test dose of 30 Gy were used. The 220 °C preheat and 200 °C cutheat temperatures were applied. The strategy of signal integration was identical to D_e estimation. The aliquots were annealed at temperatures ranging from 210 to 260 °C (interval 10 °C) with durations from 1 to 1,000 s. To make comparison, we further measured the lifetimes of OSL signals from two calibration quartz samples (180–250 μm) from Risø (batch 60 and batch 200). For the coarse-grained calibration quartz, 6 mm-diameter aliquots on stainless steel discs were used.

2.2.3 Polymineral post-IR IRSL dating

Sequences for the three pIRIR protocols are listed in Table 1. Preheat temperatures were fixed at 300 °C for the MET-$pIRIR_{250}$ protocol, and 250 °C for the $pIRIR_{225}$ and pulsed $pIRIR_{150}$ protocols. For the pulsed $pIRIR_{150}$ signal, one pulse is 500 μs (100 μs on-time and 400 μs off-time) and the gate starts from 200 to 500 μs. For the MET-$pIRIR_{250}$ protocol, pausing times of 10, 10, 20 and 40 s were applied after reaching the desired temperatures of 100, 150, 200 and 250 °C before IR stimulation to reduce the photo-transferred TL signal and also to make sure that the temperature is steady (Fu et al., 2012). For all protocols, the first 10 s of the decay curve of the pIRIR signal was used for D_e calculation with the last 10 s signal subtracted as background. For each sample, 8–12 aliquots were measured and the mean D_e was calculated. Fig. 4A shows the dose-response curve of the MET-$IRIR_{250}$ signal of a fine-grained polymineral aliquot of LUM4451.

The MET-$pIRIR_{250}$ signal is suggested to be free of anomalous fading (Li and Li, 2011), while the $pIRIR_{225}$ and pulsed $pIRIR_{150}$ signals still exhibit some degree of fading. The fading rates (g-value) of these pIRIR signals were measured following the SAR protocol (Auclair et al., 2003) with 3–4 aliquots for each sample. For the $pIRIR_{225}$ and pulsed $pIRIR_{150}$ signals, the fading correction method of Huntley and Lamothe (2001) was performed for samples younger than 50 ka (signal in the linear range of the dose-response curve)

and the fading correction method of Kars et al. (2008) was carried out for samples older than 50 ka. No fading correction was performed for the MET-pIRIR$_{250}$ signal.

Dose recovery tests were performed on several samples for pIRIR$_{225}$ and MET-pIRIR$_{250}$ protocols. For the pIRIR$_{225}$ protocol, aliquots were bleached by a solar simulator (Hönle SOL2) for 4 hours, while for the MET-pIRIR$_{250}$ protocol aliquots were bleached by the SOL2 for 48 hours. Some of the bleached aliquots were used for residual dose measurements. Three to four bleached aliquots were given a dose which was close to the D_e of the sample. These aliquots were then measured by the protocols. The recovered dose (residual dose subtracted) was divided by the given dose to obtain the DRR.

While the MET-pIRIR$_{250}$ signal is more stable compared to pIRIR$_{225}$ and pulsed pIRIR$_{150}$ signals, it is also more difficult to be bleached completely before deposition (Chen et al., 2013). An unbleachable component of the MET-pIRIR$_{250}$ signal may contribute to a residual dose for the sediments. To estimate the residual dose in nature, aliquots of different samples with 3–4 aliquots each were bleached by the SOL2 for 48 hours and the mean residual dose of each sample was measured with the MET-pIRIR$_{250}$ protocol. Residual doses were then plotted with the corresponding D_e values to obtain the residual dose contributed by the un-bleachable component (Buylaert et al., 2012; Sohbati et al., 2012; Schmidt et al., 2014; Yi et al., 2016; Abbas et al., 2023).

2.3 Magnetic susceptibility measurements

Magnetic susceptibility data is obtained by scanning with a GEOTEK multi-sensor core-logger (MSCL) equipped with a Bartington loop-sensor (MS2C) for measurement of closed cores (Federal Institute for Geosciences and Natural Resources – BGR, Hannover). The spatial resolution of magnetic susceptibility scanning is 1 cm.

3. Results

3.1 Quartz OSL ages

IR depletion ratios are within 1.00±0.05 for all quartz samples, indicating purity of the quartz fraction (Duller, 2003). The preheat test shows that the D_e values remain unchanged with the preheat temperature ranging between 160–240 °C (Fig. 5A). When the preheat temperature is above 240 °C, the D_e values start to increase with higher preheat temperature and the inter-aliquot D_e scatter becomes larger. The recycling ratios were within 10 % deviation from unity when the preheat temperature was below 240 °C, while it

becomes lower than 0.9 when the preheat temperature is above 260 °C, indicating a failure of sensitivity correction at higher preheat temperatures (Fig. 5B). As the early background subtraction is applied, the recuperation ratios are always smaller than 1 % for all preheat temperatures. Dose recovery tests (preheat temperature at 220 °C, cutheat at 200 °C) show that the given doses can be successfully recovered (Fig. 5C). These results indicate that the protocol used for quartz D_e measurements (220 °C preheat and 200 °C cutheat) is suitable. Details of dose rates and ages are listed in Tables 2 and 3, respectively.

3.2 Polymineral pIRIR ages

3.2.1 The MET-pIRIR$_{250}$ protocol

The recycling ratio is within 1.0 ± 0.1 for all pIRIR protocols and samples, and the recuperation is always <5%. For the MET-pIRIR$_{250}$ protocol, five D_e values can be measured at five different temperatures for each sample (Fig. 6A). The D_e values increase with the IR stimulation temperature as the fading rate of a pIRIR signal at a higher temperature will be smaller. If the D_e remains the same for pIRIR signals at high temperatures (e.g., 200 and 250 °C), it will be an evidence for negligible fading of these high-temperature pIRIR signals and thus no fading correction is needed. In this study, some samples (e.g., LUM4370, LUM4375, LUM 4453 and LUM 4632 in Fig. 6A) show a D_e plateau between 200 and 250 °C indicating that the MET-pIRIR$_{200}$ and MET-pIRIR$_{250}$ signals are sufficiently stable. However, for some samples the D_e still shows an increasing trend from 200 to 250 °C (Fig. 6A). In this case, it cannot be deduced whether the MET-pIRIR$_{250}$ signal is sufficiently stable or not. Fading rates of the MET-pIRIR$_{250}$ signal are measured for 6 samples. The *g*-values (t_c normalized to 2 days, g_{2d}) are quite scattered between aliquots, mostly ranging from -1.5 to +2 %/decade (Fig. 6B). This makes it difficult to judge whether there is fading or not. However, the consistency between MET-pIRIR$_{250}$ ages and fading corrected pIRIR$_{225}$ ages (next section) indicates negligible fading of the MET-pIRIR$_{250}$ signal.

The DRRs also show an increasing trend with IRSL signals stimulated at higher temperatures (Fig. 6C), which has been reported by previous studies (Kars et al., 2014; Zhang, 2018). The failure of dose recoveries for low-temperature IRSL signals (e.g., 50, 100 °C) by the MET-pIRIR$_{250}$ protocol is due to an initial sensitivity change induced by the high-temperature preheat treatment in the first cycle (Kars et al., 2014; Qin et al., 2018; Zhang, 2018). However, for the MET-pIRIR signals at 200 and 250 °C, most of the tested samples show DRRs within the acceptable range (1.0±0.1). The residual doses of the MET-pIRIR$_{250}$ signal after SOL2 bleaching show a positive relationship with corresponding D_e values of the samples (Fig. 6D). The linearly fitted line has an intercept with the y-axis, which is usually taken as the true residual dose (contributed by the un-bleachable component) of a fully bleached sample at the time of deposition (Sohbati

et al., 2012; Schmidt et al., 2014; Yi et al., 2016, Li et al., 2020; Abbas et al., 2023). This intercept residual dose (5.2 Gy) is deducted from all D_e values measured with the MET-pIRIR$_{250}$ signal. The age results are shown in Table 3.

3.2.2 The pIRIR$_{225}$ and pulsed pIRIR$_{150}$ protocol

For the pIRIR$_{225}$ signal, all tested samples show satisfactory DRRs (within 1.0 ± 0.1) except for samples LUM4370 and LUM4375, which have significantly overestimated DRRs (Fig. 7A). Fig. 7B shows a comparison between MET-pIRIR$_{250}$ ages with fading corrected pIRIR$_{225}$ ages. The fading corrected pIRIR$_{225}$ ages of LUM4370 and LUM4375 are overestimated compared to the MET-pIRIR$_{250}$ ages, while all other samples show consistency. Some studies revealed that the DRRs of the pIRIR$_{290}$ signal were overestimated when a hot-bleach was added at the end of the SAR cycle, whereas the DRRs were close to unity without the hot-bleach (Wacha et al., 2015; Lauer et al., 2017). Here, we perform dose recovery tests for the pIRIR$_{225}$ signal without hot-bleach (Step 9 in the pIRIR$_{225}$ protocol in Table 1) for LUM4370 and LUM4375 and the DRRs are reduced to 1.08±0.01 and 0.99±0.01, respectively (Fig. 7A). The pIRIR$_{225}$ D_e values of LUM4370 and LUM4375 have also been repeatedly measured without hot-bleach. The fading corrected pIRIR$_{225}$ age of LUM4375 without hot-bleach becomes consistent with the MET-pIRIR$_{250}$ age (Fig. 7B). The fading corrected pIRIR$_{225}$ age of LUM4370 without hot-bleach becomes closer to the MET-pIRIR$_{250}$ age, but is still overestimated (Fig. 7B), which aligns with the slightly overestimated DRR (1.08±0.01). Notably, dose recovery tests without hot-bleach performed on three younger samples (LUM4607, 4631, 4632) yield DRRs similar to those with hot-bleach (Fig. 7A).

Fig. 7C shows the *g*-values of 4 aliquots of sample LUM4453 and Fig. 7D the fading correction of the pIRIR$_{225}$ age following Kars et al. (2008). It should be noted that a small laboratory dose of ~70 Gy is used for all samples for *g*-value measurements. Previous studies reveal that the measured *g*-values increase with larger laboratory doses used for the *g*-value measurements (Huntley and Lian, 2006; Li and Li, 2008; Lomax et al., 2022). As the model of Kars et al. (2008) has already incorporated the fading rate change with increasing irradiation, a small laboratory dose should be used to measure the initial fading rate.

For pIRIR$_{225}$ and pulsed pIRIR$_{150}$ signals, the residual doses of well-bleached samples should be much lower than the MET-pIRIR$_{250}$ signal (5.2±0.3 Gy), as lower stimulation temperatures and preheat temperatures are used. Thus, the residual doses are negligible and no residual doses have been subtracted from the D_e values of the pIRIR$_{225}$ and pulsed pIRIR$_{150}$ signals. Apparent ages and fading corrected ages are listed in Table 4.

3.3 Comparison of ages obtained by different luminescence signals

Quartz OSL ages and polymineral pIRIR ages are plotted against composite depth (Fig. 8A). For the uppermost sample at 0.5 m depth, the quartz OSL age is younger than 1 ka. This age may not represent the sediment deposition age as the sample is located in close proximity to the surface, and human activity (e.g. agriculture) could disrupt the sediments and reset the luminescence signal. For samples between 1.0 and 3.0 m depth with ages younger than 45 ka, quartz OSL ages and polymineral pIRIR ages are consistent with each other, except for sample LUM4629 at 1.0 m depth, for which the MET-$pIRIR_{250}$ age is about 5 ka older than the quartz OSL age. Given the relatively faster bleaching rate of the quartz OSL signal compared to polymineral pIRIR signals, the agreement between OSL and pIRIR ages suggests that both the OSL and pIRIR signals of the sediments were completely bleached prior to deposition. For samples situated below 3.4 m depth, polymineral pIRIR ages are older than 70 ka and quartz OSL ages become systematically younger compared to pIRIR ages (Fig. 8A). As the three pIRIR signals with different bleachability (pulsed $pIRIR_{150}$, $pIRIR_{225}$, MET-$pIRIR_{250}$) still generate consistent ages, the three pIRIR signals of the sediments were completely bleached before deposition. The discrepancy between quartz OSL ages and polymineral pIRIR ages should be a result of quartz OSL age underestimation.

The trap depths (E) and frequency factors (*s*) estimated from isothermal annealing tests on Rodderberg quartz are listed in Table 5. For one aliquot of LUM4608, thirteen annealing temperatures ranging from 210 to 270 °C with an interval of 5 °C were applied. The E and *s* values deduced from thirteen annealing temperatures are similar to those deduced from six annealing temperatures ranging from 210 to 260 °C with an interval of 10 °C (Fig. 9). Therefore, we propose that the six annealing temperatures employed for all other aliquots are adequate to yield reliable estimates. Based on the E and *s* values, the lifetimes at 20 °C (τ_{20}) for the two Rodderberg samples (LUM4608 and LUM4632) are calculated to be 54 Ma and 73 Ma, respectively, showing the thermal stability of quartz OSL signal.

Fading corrected $pIRIR_{225}$ ages and pulsed $pIRIR_{150}$ ages are generally consistent with the MET-$pIRIR_{250}$ ages (Fig. 7B). Being exposed to sunlight, the pulsed $pIRIR_{150}$ bleaches faster than the $pIRIR_{225}$ signal and the MET-$pIRIR_{225}$ signal bleaches slowest. If the sediments were partially bleached before burial, the MET-$pIRIR_{250}$ signal would have the highest residual dose and exhibit the oldest age, while the pulsed $pIRIR_{150}$ signal would show the youngest age. Here, the consistency of ages between the three pIRIR signals until a depth of 37.5 m is a good evidence of complete signal resetting before burial of the sediments.

For the ten samples below 37.5 m depth, the MET-$pIRIR_{250}$ ages stop to increase with depth and cluster at ca. 250 ka (Fig. 10). Five samples below 37.5 m depth have also been dated with the $pIRIR_{225}$ protocol.

The fading corrected $pIRIR_{225}$ ages are deviated from the MET-$pIRIR_{250}$ ages. For the three samples at depths of 47, 58 and 70 m, the fading corrected $pIRIR_{225}$ ages are 321±39 ka, 326±41 ka, and 774±144 ka, respectively. However, as the fading corrected D_e values are already beyond the $2D_0$ limit, these fading corrected $pIRIR_{225}$ ages cannot be regarded as reliable. Overall, the sediments below 37.5 depth are beyond the dating limits of the protocols used in this study.

3.4 Age–depth modelling

An age-depth model for the composite sediment core ROD11 above 37.5 m depth is built with the rBacon package (Blaauw and Christen, 2011). For samples below 37.5 m depth, there are only minimum ages. Accordingly, they are not considered for age-depth modelling. The uppermost sample at 0.5 m depth has likely been disturbed by human activities. Thus, it is not used for modelling either. For depths between 1.0 and 3.0 m (ages < 45 ka), only quartz OSL ages are used for modelling, while for the section between 3.0 and 37.5 m depth, all three kinds of pIRIR ages (MET-$pIRIR_{250}$, $pIRIR_{225}$ and pulsed $pIRIR_{150}$) are applied for age-depth modelling. Notably, $pIRIR_{225}$ ages are measured both with and without hot-bleach for samples LUM4370 and LUM4375. Only the $pIRIR_{225}$ age without hot-bleach for LUM4375 is applied for modelling.

A hiatus located between 3.8–4.8 m is assumed. Therefore, ROD11 is divided into two segments for Bacon modelling, with segment 1 of 1.0–3.8 m and segment 2 of 4.8–37.5 m. Based on the observation of abrupt changes in sedimentation rates for segment 1, two boundaries are set at 2.0 and 3.0 m, respectively. The prior sedimentation rates are set as 20, 4 and 1 cm/ka for the three intervals according to linear fitting of measured ages and depth. For segment 2, a boundary is set at 10.0 m based on an abrupt change in sedimentation rates. The prior sedimentation rate is set as 20 cm/ka for the interval of 10.0–37.5 m according to linear fitting. However, linear fitting for the interval of 4.8–10.0 m generates a negative sedimentation rate as the ages are too close to each other. Consequently, a prior sedimentation rate of 200 cm/ka is artificially set for this interval. Bacon divides the core into sections of equal thickness for modelling. This thickness is set as 10 cm for segment 1 and 20 cm for segment 2, respectively. The results of the modelling are shown in Fig. 10 together with measured ages.

4. Discussion

4.1 Dating limits for the luminescence signals

Conventionally, two times of the characteristic saturation dose (D_0) of a luminescence signal is taken as the dating limit of this signal, beyond which reliable D_e cannot be measured (Wintle and Murray, 2006). For quartz samples in this study we construct dose-response curves with a maximum regenerative dose of up to 650 Gy. The D_0 values are mostly in the region of 180–230 Gy (Fig. 8B), which means that reliable D_e values can be obtained theoretically up to ~400 Gy. However, OSL ages start to be underestimated when the D_e is above 156 Gy (Fig. 8B). The occurrence of quartz D_e underestimation, which commences at significantly lower doses (e.g., 150–200 Gy), as opposed to the $2D_0$ limit, has been documented for various regions across the world, such as the Chinese Loess Plateau (Buylaert et al., 2007; Roberts, 2008; Lai, 2010; Chapot et al., 2012; Timar-Gabor et al., 2017; Perić et al., 2019; Wang et al., 2021), Serbia (Perić et al., 2019, 2022), Romania (Timar-Gabor et al., 2011, 2017; Constantin et al., 2014) and Israel (Faershtein et al., 2019). Abnormally short lifetimes of OSL signal have been reported for quartz samples from the Chinese Loess Plateau and the neighboring Mu Us desert, which could result in D_e underestimation (Fan et al., 2011; Lai and Fan, 2014). The lifetimes (τ_{20}) for the two tested Rodderberg samples (LUM4608 and LUM4632) are 54 Ma and 73 Ma, respectively. These long lifetimes indicate that the underestimation of quartz D_e at Rodderberg is not due to low signal stability, but rather to the divergence between the dose-response curves of the natural environment and those established under laboratory conditions (Chapot et al., 2012; Timar-Gabor and Wintle, 2013; Timar-Gabor et al., 2015; Wang et al., 2021; Peng et al., 2022).

For the sediments below 37.5 m depth, the MET-$pIRIR_{250}$ ages almost don't increase with depth, and lie around 250 ka (Fig. 10). Such kind of age 'saturation' has also been reported for coarse-grained K-feldspar samples in previous studies, when the samples meet the dating limit (e.g., Li et al., 2020; Zhang et al., 2022). The $2D_0$ values are plotted with the D_e values of the samples, and the $2D_0$ values are generally around 800 Gy (Fig. 11). With the increasing sample depth, D_e values gradually increase and become very close to 800 Gy below 40 m depth. Thus, the MET-$pIRIR_{250}$ ages in the lower part of the core can only be regarded as the minimum ages of the sediments. The three samples at depths of 47, 58 and 70 m have fading corrected $pIRIR_{225}$ ages of 321±39 ka, 326±41 ka, and 774±144 ka, respectively. However, fading correction can bring in large error when the sample is old. Empirically, when the fading corrected age is older than the $2D_0$ age, i.e. the age when the fading corrected D_e equals to $2D_0$, it cannot be regarded as reliable. Taking $2D_0$ ages as the minimum ages, the minimum $pIRIR_{225}$ age at 47 m (LUM4373) would be 287±16 ka (Table 4).

4.2 Age framework

The eruption age of the Rodderberg volcano can provide maximum age control for the crater sediments as the sediments lie directly above the Rodderberg volcaniclastic and volcanic rocks (Zolitschka et al., 2014). However, eruption ages deduced indirectly based on the stratigraphy of Rodderberg tephra in the nearby loess sequences and fluvial terraces give contradictory results, such as 30 ka (Remy, 1960), 370–250 ka (Hard, 1973, 1974) and ca. 500 ka (Boenigk and Frechen, 2006). Ages obtained by absolute dating of a siltstone xenolith and phreatomagmatic tuff with TL indicate an eruption prior to 300 ka (Blanchard, 2002; Paulick et al., 2009; Zöller and Blanchard, 2009).

Our pIRIR dating of the lower part of the core ROD11 (72.8–37.5 m) failed to generate reliable ages, as the sediments are already beyond the limits of the dating methods applied in this study. Nevertheless, our pIRIR ages provide some constraints as they are regarded as minimum ages. It is evident that the sediments below 37.5 m should be older than 250 ka (Fig. 10). Moreover, based on the fading corrected $pIRIR_{225}$ age of the sample from 47 m (LUM4373), the sediment below 47 m should be older than 287±16 ka. Thus, our pIRIR ages of crater sediments are consistent with previous TL dating results indicating an eruption age of > 300 ka (Blanchard, 2002; Paulick et al., 2009; Zöller and Blanchard, 2009). Blanchard (2002) dated one sediment sample from 50 m depth of core KB1, which generated fading uncorrected TL and IRSL ages of 106.5±26.7 ka and 66.3±13.1 ka, respectively. These two ages are significantly smaller than ages indicated by our dating results (>250 ka). This should be the result of fading induced age underestimation as suggested by Zöller et al. (2002).

Based on geochemical and pollen analyses, Zolitschka et al. (2014) suggested that the record from Rodderberg covers at least the last three glacial-interglacial cycles. According to the pollen biostratigraphy of Schläfli et al. (2023), the lowermost Rodderberg interglacial (LRI) at a depth of 69.0 to 61.3 m should not be correlated to MIS 7 but most likely to MIS 11, although a correlation with MIS 9 cannot be completely excluded. Our luminescence dating results indicate that the sediment below 37.5 m is older than MIS 7 supporting the pollen-based interpretation of Schläfli et al. (2023).

From 37.5 to 23.6 m, Bacon ages range from 257±11 to 190±8 ka and correlates to MIS 7 (Fig. 10). Furthermore, this correlation is supported by the paired peaks in magnetic susceptibility for this interval, which is nicely comparable with the benthic $\delta^{18}O$ record (Lisiecki and Raymo, 2005). The higher magnetic susceptibility in lake sediments during interglacial periods might be due to enhanced slop washing which brought more basaltic rock fragments into the lake. Note that the upper boundary at 23.6 m depth is set based on a mean Bacon age of 190 ka. Considering the error of Bacon age, the upper boundary can shift between 21.9 and 25.2 m depths. From 23.6 to 10.0 m, the Bacon ages range from 190±8 ka to 132±4 ka corresponding to MIS 6 (Fig. 10). The ages grow linearly with depth between 37.5–10.0 m indicating a constant sedimentation rate.

For sediments in the interval between 10.0 and 4.0 m, measured ages are indistinguishable from each other (Fig. 12). Following the Bacon age-depth model, mean Bacon ages range from 132.0 to 129.4 ka, which is at the transition from the penultimate glacial (MIS 6) to the last interglacial (MIS 5e). The remarkably identical ages during this interval imply an extremely high dust sedimentation rate.

From 3.8 to 1.0 m, Bacon ages range from 115±14 to 13.2±1.3 ka corresponding to the Weichselian glaciation (Fig. 12). For sediments collected at 0.5 m depth, the quartz OSL age is 0.91±0.04 ka and the feldspar MET-pIRIR$_{250}$ age 2.6±0.1 ka. We propose that these relatively recent ages do not reflect original deposition but rather have been influenced by human impact (agriculture) and/or pedogenetic processes, leading to a resetting of luminescence signals.

4.3 The missing Eemian

The Bacon age at 3.8 m (115±11 ka) has a large error because of a low sedimentation rate at this interval. However, the measured MET-pIRIR$_{250}$ and pIRIR$_{225}$ ages are 115.5±7.0 and 116.6±6.9 ka, respectively, which are almost identical. We take the mean of measured ages (116±5 ka) at this depth for the following discussion. The ages increase from 116±5 ka at 3.8 m to 129±4 ka at 4.8 m bracketing the Eemian period (128–115ka). The Eemian interglacial had an annual temperature warmer than present-day (Kukla et al., 2002), which should cause the formation of a soil by intensified pedogenesis. However, the low magnetic susceptibility between 4.8–3.8 m shows no signs of soil formation or wetter climatic conditions indicating that the Eemian record is missing at Rodderberg (Fig. 12). As Eemian soils have been recorded for many sites in the European loess belt (Lehmkuhl et al., 2016), such as the loess-palaeosol sequences at Tönchesberg and Koblenz-Metternich (Boenigk and Frechen, 2001; Schmidt et al., 2011a) in a distance of only 35 km S from Rodderberg, it is unlikely that there was no Eemian pedogenesis at Rodderberg, especially if considering that the bowl-shaped crater basin acts as a sediment trap. Thus, the lack of any signs of soil formation suggests that an erosional event removed the Eemian soil. The erosional hiatus should exist between 4.8–3.8 m. However, if the hiatus is located below 4.0 m, based on the sedimentation rate between 3.8–3.0 m (1 cm/ka), the age would be ca. 136 ka at 4.0 m, which is even larger than the Bacon ages between 10.0–4.8 m. The sediments at the interval of 4.0–3.8 m would be expected to span an age range of 136–116 ka bracketing the Eemian, and thus have high magnetic susceptibility. However, magnetic susceptibility between 4.0–3.8 m is very low (Fig. 12). These controversies suggest that the hiatus should be located between 4.0–3.8 m, and the sediments between 4.8–4.0 m should have similar ages (ca. 129 ka) as the 10.0–4.8 m interval. The low magnetic susceptibility between 4.8–4.0 m further supports this interpretation.

The age of 116±5 ka at 3.8 m indicates that the erosion happened soon after the Eemian. A late Eemian Aridity Pulse (LEAP) lasting for 468 years at ca. 118 ka was identified from the Eifel laminated sediment archive (ELSA) for the West Eifel Volcanic Field (Sirocko et al., 2005). The presence of larger quartz grainsizes and increased levels of loess within the varved sediments during the LEAP suggests the occurrence of stronger winds and frequent dust storms during that period (Sirocko et al., 2005). We suggest that the LEAP event might have caused erosion of the Eemian soil at Rodderberg.

The following scenario is proposed:

1) Before ca. 160 ka (below 17 m depth in ROD11), a lake existed in the crater and lake sediments accumulated from the crater bottom to 17 m depth.
2) After ca. 160 ka, the lake dried out and aeolian dust (loess) started to accumulate inside the crater basin. The crater basin became shallower with time.
3) During the Eemian, there was almost no dust accumulation. Due to a more oceanic climate with warmer temperatures and higher precipitation, pedogenesis caused the formation of an Eemian soil.
4) At the end of Eemian, wind activity was strong during the LEAP. These intense winds have the capacity to transport dust particles into the crater, yet they can also induce erosion of sediments. The balance between sediment loss and gain within the crater basin hinges on the interplay between the two opposing factors of accumulation and erosion. As the depth of the silted-up crater basin was already too shallow to prevent from wind erosion, topmost sediments were blown out by wind turbulence (Fig. 13). Thus, the Eemian soil and potentially some older loess deposited prior to the Eemian were eroded.
5) During the Weichselian, dust started to accumulate again inside the crater. However, this happened with a much lower sedimentation rate (mean value of 2.7 cm/ka) compared to MIS 6 (24 cm/ka) and the transition stage (200 cm/ka) suggesting that tenfold less accumulation occurred during the Weichselian. Assuming comparable sedimentation rates for the different glacials, this would indicate that the Weichselian glacial is characterized not only by dust accumulation but also by a considerable number of erosional events with the maximum of erosion right at the beginning, when the Eemian soil was eroded.

A missing Eemian soil is also reported for nearby loess sections, such as Ariendorf (ca. 13 km S of Rodderberg) and Kärlich (ca. 35 km S of Rodderberg) (Schmidt et al., 2014). Notably, Kärlich is within 10 km distance of Tönchesberg and Koblenz-Metternich, but the latter two loess sections have preserved Eemian soils. This indicates that loess deposition and erosion in the East Eifel and the Middle Rhine area are strongly affected by local environmental conditions.

4.4 Sedimentation rates

Sedimentation rate is an indicator of past atmospheric dust activity, which can hold palaeoclimatic information (Frechen et al., 2003; Kang et al., 2015; Perić et al., 2019). We calculate sedimentation rates for ROD11 based on the Bacon age-depth model (Fig. 14).

Lithological investigation indicates that the sediments in the Rodderberg basin below 17 m depth are layered deposits, which implies a lake or at least moist conditions (swamp). Such an environment will favor continuous deposition without hiatus. Above 17 m, it changes to dry (aeolian) deposition and wind erosion may intercalate the deposition.

The sedimentation rates between 250 and 130 ka (37.5–10 m) are quite steady with values of 19–25 cm/ka and much higher than during the Weichselian (mean value of 2.7 cm/ka). This is partially caused by the morphology of the Rodderberg. The shape of the crater basin is like a funnel. The area for trapping dust is always the same, determined by the crater diameter. In an early stage of deposition, when dust fills the basin, the area for dust settling is relatively small. Dust deposited on the steep crater walls is flushed down to the bottom of the basin resulting in higher sedimentation rates at its centre compared to a flat landscape – a process called “sediment focusing”. Moreover, the deposition below 17 m is under a lacustrine environment, which prevents wind erosion; while the loess deposits at a dry environment during the Weichselian are easily affected by wind erosion. The generally constant sedimentation rate between 37.5–10 m also indicates continuous dust accumulation with no hiatus in the centre of the Rodderberg crater basin during the penultimate glacial-interglacial cycle (MIS 7–6).

During the Weichselian (3.8–1.0 m) sedimentation rates decrease significantly. This happens if a theoretical point is reached at which the process of sediment focusing terminates due to silting-up of the crater basin. At this point not only sediment focusing comes to an end but also – as the elevation of the central bottom of the crater basin can potentially reach the crater rim – a shift from deposition only to deposition alternating with erosion takes place. Consequently, this shift reduces sedimentation rates considerably. Sedimentation rates during the last glacial at Rodderberg are compared with adjacent loess sections of the Middle Rhine Valley (Fig. 14): Ringen (Zens et al., 2018), Schwalbenberg (Frechen and Schirmer, 2011; Klasen et al., 2015), Tönchesberg (Frechen et al., 2003) and Koblenz-Metternich (Frechen et al., 2003), all show that the sedimentation rate at Rodderberg is much lower, which provides further evidence for the occurrence of erosional events at Rodderberg during the last glacial. Notably, the very high sedimentation rates at the Schwalbenberg core section (Klasen et al., 2015) and Koblenz-Metternich

(Frechen et al., 2003) might be related to enhanced fluvio-aeolian recycling of silt-rich material during glacial periods (Frechen et al., 2003).

Between 10.0–4.0 m, with Bacon ages ranging from 132±4 to 129±4 ka, the sedimentation rate is extremely high, up to 200 cm/ka. During MIS 6, the maximum ice-sheet cover over Eurasia was in the Late Saalian (160–140 ka) (Svendsen et al., 2004), which corresponds to a depth of 17.0–12.2 m for ROD11. However, the highest sedimentation rate at Rodderberg occurs between 132–129 ka during deglaciation. This phenomenon could potentially arise from an intensified 'sediment focusing' effect. During this transitional period, as temperatures increased, the thawing permafrost triggered the movement of sediments from the crater walls toward the centre of the crater, driven by slope-wash and solifluction. The solifluction process is commonly observed for loess deposits of the Middle Rhine Area (Boenigk and Frechen, 2001), as well as in modern-day Arctic soils (Glade et al., 2021). An alternate explanation could be that the elevated sedimentation rate is a terrestrial representation of Heinrich event 11 (Heinrich, 1988). The North Atlantic cold anomaly preceding the last interglacial period could have triggered strong winds across Central Europe resulting in a substantial flux of aeolian dust into the Rodderberg crater. Detailed lithologic investigations are ongoing to obtain more certainty with this interpretation.

5. Conclusions

Our dating provides detailed age constraints for the 72.8 m-long sediment core ROD11 from the Rodderberg crater basin. The ages increase from 13 ka at 1.0 m to ca. 250 ka at 37.5 m depth. Due to limitations of the dating protocols, reliable ages cannot be obtained for the lower half of the core (72.8–37.5 m). Nevertheless, it is evident that these sediments have been deposited prior to 250 ka.

The agreement among the three pIRIR ages from polymineral samples is a strong evidence for the credibility of determined ages. Furthermore, the concordance between quartz OSL ages and pIRIR ages for the last 50 ka further demonstrates that the sediments were effectively bleached prior to deposition. However, quartz OSL ages start to show underestimations compared to pIRIR ages when the quartz D_e is beyond 156 Gy (i.e. for ages beyond 45 ka), which is the result of a discrepancy between quartz natural and laboratory dose-response curves in the high dose range.

The absence of the Eemian soil at Rodderberg points to an erosional event that occurred during the Late Eemian Aridity Pulse at around 118 ka. The constant sedimentation rate observed throughout MIS 7–6 indicates continuous dust accumulation during the penultimate glacial-interglacial cycle. However, sedimentation rates of MIS 7–6 (ca. 20 cm/ka) are much higher compared to the Weichselian (mean: 2.7

cm/ka). The high sedimentation rate during MIS 7–6 are likely the result of sediment focusing – dust deposited on the crater walls being flushed downward to the bottom of the basin. The low sedimentation rate during the Weichselian might be related to both the termination of sediment focusing and multiple erosional events alternating with deposition, as the elevation of the crater basin was getting closer to the crater rim. The extremely high sedimentation rate (ca. 200 cm/ka) at the transition from MIS 6 to MIS 5e at 132–129 ka (10.0–4.0 m) could either be related to intensified sediment focusing resulting from permafrost thawing or intensified input of aeolian dust due to strong winds during Heinrich event 11. Further studies are ongoing for clarification.

Acknowledgements

The authors thank Sonja Riemenschneider for the help in sample preparation and Petra Posimowski in gamma spectrometry measurements. This study is funded by the Deutsche Forschungsgemeinschaft (DFG, German Research Foundation) as project number 420499726.

References

Abbas, W., Zhang, J., Tsukamoto, S., Ali, S., Frechen, M., Reicherter, K., 2023. Pleistocene-Holocene deformation and seismic history of the Kalabagh Fault in Pakistan using OSL and post-IR IRSL dating. Quat. Int. 651, 42–61. https://doi.org/10.1016/j.quaint.2022.01.007

Auclair, M., Lamothe, M., Huot, S., 2003. Measurement of anomalous fading for feldspar IRSL using SAR. Radiat. Meas. 37, 487–492. https://doi.org/10.1016/S1350-4487(03)00018-0

Bartels, G., Hard, G., 1974. Zur Datierung des Rodderbergs bei Bonn. Decheniana 126 (1973/1974), 367–376.

Bartels, G., Hard, G., 1973. Rodderbergtuff im Rheinischen Quartärprofi l. Zur zeitlichen Stellung des Rodderberg-Vulkanismus. CATENA 1, 31–56.

Bibus, E., 1980. Zur Relief-, Boden- und Sedimententwicklung am unteren Mittelrhein. Frankf. Geowiss. Arb., D 1, 1–296.

Bittmann, F., 1992. The K€arlich interglacial, Middle Rhine region, Germany: vegetation history and stratigraphic position. Veg. Hist. Archaeobotany 1, 243–258. https://doi.org/10.1007/bf00189501.

Blaauw, M., Christen, J.A., 2011. Flexible Paleoclimate Age-Depth Models Using an Autoregressive Gamma Process. Bayesian Anal. 6, 457–474.

Blanchard, H., 2002. Neue Erkenntnisse zur Eruptions und Landschaftsgeschichte des Rodderbergs bei Bonn (Unpublished Diploma thesis). Geographisches Institut der Rheinischen Friedrich- Wilhelms-Universität Bonn.

Boenigk, W., Frechen, M., 2006. The Pliocene and Quaternary fluvial archives of the Rhine system. Quat. Sci. Rev. 25, 550–574. https://doi.org/10.1016/j.quascirev.2005.01.018

Boenigk, W., Frechen, M., 2001. The loess record in sections at Koblenz–Metternich and Tönchesberg in the Middle Rhine Area. Quat. Int. 76–77, 201–209. https://doi.org/10.1016/S1040-6182(00)00103-8

Brennan, B.J., Lyons, R.G., Phillips, S.W., 1991. Attenuation of alpha particle track dose for spherical grains. Int. J. Radiat. Appl. Instrum. Part Nucl. Tracks Radiat. Meas. 18, 249–253. https://doi.org/10.1016/1359-0189(91)90119-3

Buylaert, J.-P., Jain, M., Murray, A.S., Thomsen, K.J., Thiel, C., Sohbati, R., 2012. A robust feldspar luminescence dating method for Middle and Late Pleistocene sediments: Feldspar luminescence dating of Middle and Late Pleistocene sediments. Boreas 41, 435–451. https://doi.org/10.1111/j.1502-3885.2012.00248.x

Buylaert, J.P., Murray, A.S., Thomsen, K.J., Jain, M., 2009. Testing the potential of an elevated temperature IRSL signal from K-feldspar. Radiat. Meas. 44, 560–565. https://doi.org/10.1016/j.radmeas.2009.02.007

Buylaert, J.P., Vandenberghe, D., Murray, A.S., Huot, S., De Corte, F., Van den Haute, P., 2007. Luminescence dating of old (> 70 ka) Chinese loess: A comparison of single-aliquot OSL and IRSL techniques. Quat. Geochronol. 2, 9–14. https://doi.org/10.1016/j.quageo.2006.05.028

Chapot, M.S., Roberts, H.M., Duller, G.A.T., Lai, Z.P., 2012. A comparison of natural- and laboratory-generated dose response curves for quartz optically stimulated luminescence signals from Chinese Loess. Radiat. Meas. 47, 1045–1052. https://doi.org/10.1016/j.radmeas.2012.09.001

Chen, Y., Li, S.-H., Li, B., 2013. Residual doses and sensitivity change of post IR IRSL signals from potassium feldspar under different bleaching conditions. Geochronometria 40, 229–238. https://doi.org/10.2478/s13386-013-0128-3

Constantin, D., Begy, R., Vasiliniuc, S., Panaiotu, C., Necula, C., Codrea, V., Timar-Gabor, A., 2014. High-resolution OSL dating of the Costineşti section (Dobrogea, SE Romania) using fine and coarse quartz. Quat. Int. 334–335, 20–29. https://doi.org/10.1016/j.quaint.2013.06.016

De Corte, F., Vandenberghe, D., De Wispelaere, A., Buylaert, J.-P., Van Den Haute, P., 2006. Radon loss from encapsulated sediments in Ge gamma-ray spectrometry for the annual radiation dose determination in luminescence dating. Czechoslov. J. Phys. 56, D183–D194. https://doi.org/10.1007/s10582-006-1016-3

Duller, G.A.T., 2003. Distinguishing quartz and feldspar in single grain luminescence measurements. Radiation Measurements 37, 161–165. https://doi.org/10.1016/S1350-4487(02)00170-1

Fan, A., Li, S.-H., Li, B., 2011. Observation of unstable fast component in OSL of quartz. Radiat. Meas. 46, 21–28. https://doi.org/10.1016/j.radmeas.2010.10.001

Faershtein, G., Porat, N., Matmon, A., 2019. Natural saturation of OSL and TT-OSL signals of quartz grains from Nilotic origin. Quaternary Geochronology 49, 146–152. https://doi.org/10.1016/j.quageo.2018.04.002

Fischer, S., 2004. Würmlöß-Stratigraphie undTephrochronologie zur Erschließung problematischer Geoarchivein Kratern –dargestellt am Beispiel des Rodderbergs bei Bonn (Dipl.-Arb). Geographisches Institut, Bonn.

Frechen, M., Schirmer, W., 2011. Luminescence Chronology of the Schwalbenberg II Loess in the Middle Rhine Valley. E&G Quaternary Sci. J. 60, 78–89. https://doi.org/10.3285/eg.60.1.05

Frechen, M., Oches, E.A., Kohfeld, K.E., 2003. Loess in Europe—mass accumulation rates during the Last Glacial Period. Quat. Sci. Rev. 22, 1835–1857. https://doi.org/10.1016/S0277-3791(03)00183-5

Fu, X., Li, B., Li, S.-H., 2012. Testing a multi-step post-IR IRSL dating method using polymineral fine grains from Chinese loess. Quaternary Geochronology 10, 8–15. https://doi.org/10.1016/j.quageo.2011.12.004

Glade, R.C., Fratkin, M.M., Pouragha, M., Seiphoori, A., Rowland, J.C., 2021. Arctic soil patterns analogous to fluid instabilities. Proc. Natl. Acad. Sci. U.S.A. 118, e2101255118. https://doi.org/10.1073/pnas.2101255118

Heinrich, H., 1988. Origin and Consequences of Cyclic Ice Rafting in the Northeast Atlantic-Ocean during the Past 130,000 Years. Quat. Res. 29, 142–152.

Huntley, D.J., Lamothe, M., 2001. Ubiquity of anomalous fading in K-feldspars and the measurement and correction for it in optical dating. Can. J. Earth Sci. 38, 1093–1106. https://doi.org/10.1139/e01-013

Huntley, D.J., Lian, O.B., 2006. Some observations on tunnelling of trapped electrons in feldspars and their implications for optical dating. Quat. Sci. Rev. 25, 2503–2512. https://doi.org/10.1016/j.quascirev.2005.05.011

Kang, S.G., Roberts, H.M., Wang, X.L., An, Z.S., Wang, M., 2015. Mass accumulation rate changes in Chinese loess during MIS 2, and asynchrony with records from Greenland ice cores and North Pacific Ocean sediments during the Last Glacial Maximum. Aeolian Res. 19, 251–258.

Kars, R.H., Reimann, T., Wallinga, J., 2014. Are feldspar SAR protocols appropriate for post-IR IRSL dating? Quat. Geochronol. 22, 126–136. https://doi.org/10.1016/j.quageo.2014.04.001

Kars, R.H., Wallinga, J., Cohen, K.M., 2008. A new approach towards anomalous fading correction for feldspar IRSL dating — tests on samples in field saturation. Radiat. Meas. 43, 786–790. https://doi.org/10.1016/j.radmeas.2008.01.021

Klasen, N., Fischer, P., Lehmkuhl, F., Hilgers, A., 2015. Luminescence dating of loess deposits from the Remagen-Schwalbenberg site, Western Germany. Geochronometria 42. https://doi.org/10.1515/geochr-2015-0008

Klostermann, J., Holl, C., v. d. Logt, S., 2000. Schichtenverzeichnis der Kartierbohrung Rodderberg I. Ber. Geol. Dienst NRW 1–13.

Kreutzer, S., Fuchs, M., Meszner, S., Faust, D., 2012. OSL chronostratigraphy of a loess-palaeosol sequence in Saxony/Germany using quartz of different grain sizes. Quat. Geochronol. 10, 102–109. https://doi.org/10.1016/j.quageo.2012.01.004

Kreutzer, S., Schmidt, C., DeWitt, R., Fuchs, M., 2014. The a-value of polymineral fine grain samples measured with the post-IR IRSL protocol. Radiat. Meas. 69, 18–29. https://doi.org/10.1016/j.radmeas.2014.04.027

Kukla, G.J., Bender, M.L., De Beaulieu, J.-L., Bond, G., Broecker, W.S., Cleveringa, P., Gavin, J.E., Herbert, T.D., Imbrie, J., Jouzel, J., Keigwin, L.D., Knudsen, K.-L., McManus, J.F., Merkt, J., Muhs, D.R., Müller, H., Poore, R.Z., Porter, S.C., Seret, G., Shackleton, N.J., Turner, C., Tzedakis, P.C., Winograd, I.J., 2002. Last Interglacial Climates. Quat. Res. 58, 2–13. https://doi.org/10.1006/qres.2001.2316

Lai, Z., 2010. Chronology and the upper dating limit for loess samples from Luochuan section in the Chinese Loess Plateau using quartz OSL SAR protocol. J. Asian Earth Sci. 37, 176–185. https://doi.org/10.1016/j.jseaes.2009.08.003

Lai, Z.P., Fan, A.C., 2014. EXAMINING QUARTZ OSL AGE UNDERESTIMATION FOR LOESS SAMPLES FROM LUOCHUAN IN THE CHINESE LOESS PLATEAU. Geochronometria 41, 57–64. https://doi.org/10.2478/s13386-013-0138-1

Lauer, T., Frechen, M., Vlaminck, S., Kehl, M., Lehndorff, E., Shahriari, A., Khormali, F., 2017. Luminescence-chronology of the loess palaeosol sequence Toshan, Northern Iran – A highly resolved climate archive for the last glacial–interglacial cycle. Quat. Int. 429, 3–12. https://doi.org/10.1016/j.quaint.2015.03.045

Lehmkuhl, F., Zens, J., Krauß, L., Schulte, P., Kels, H., 2016. Loess-paleosol sequences at the northern European loess belt in Germany: Distribution, geomorphology and stratigraphy. Quat. Sci. Rev. 153, 11–30. https://doi.org/10.1016/j.quascirev.2016.10.008

Lehmkuhl, F., Pötter, S., Pauligk, A., Bösken, J., 2018. Loess and other Quaternary sediments in Germany. Journal of Maps 14, 330–340. https://doi.org/10.1080/17445647.2018.1473817

Li, B., Li, S.-H., 2011. Luminescence dating of K-feldspar from sediments: A protocol without anomalous fading correction. Quat. Geochronol. 6, 468–479. https://doi.org/10.1016/j.quageo.2011.05.001

Li, B., Li, S.-H., 2008. Investigations of the dose-dependent anomalous fading rate of feldspar from sediments. J. Phys. Appl. Phys. 41, 225502. https://doi.org/10.1088/0022-3727/41/22/225502

Li, G., Yang, H., Stevens, T., Zhang, X., Zhang, H., Wei, H., Zheng, W., Li, L., Liu, X., Chen, J., Xia, D., Oldknow, C., Ye, W., Chen, F., 2020. Differential ice volume and orbital modulation of Quaternary moisture patterns between Central and East Asia. Earth Planet. Sci. Lett. 530, 115901. https://doi.org/10.1016/j.epsl.2019.115901

Liritzis, I., Stamoulis, K., Papachristodoulou, C., Ioannides, K., 2013. A RE-EVALUATION OF RADIATION DOSE-RATE CONVERSION FACTORS. Mediterr. Archaeol. Archaeom., SpringerBriefs in Earth System Sciences 13, 1–15. https://doi.org/10.1007/978-3-319-00170-8_3

Lisiecki, L.E., Raymo, M.E., 2005. A Pliocene-Pleistocene stack of 57 globally distributed benthic δ ^{18} O records: PLIOCENE-PLEISTOCENE BENTHIC STACK. Paleoceanography 20, n/a-n/a. https://doi.org/10.1029/2004PA001071

Liu, T., Ding, Z., 1998. CHINESE LOESS AND THE PALEOMONSOON. Annu. Rev. Earth Planet. Sci. 26, 111–145. https://doi.org/10.1146/annurev.earth.26.1.111

Lomax, J., Wolf, D., Meliksetian, K., Wolpert, T., Sahakyan, L., Hovakimyan, H., Faust, D., Fuchs, M., 2022. Testing post-IR-IRSL dating on Armenian loess-palaeosol sections against independent age control. Quat. Geochronol. 69, 101265. https://doi.org/10.1016/j.quageo.2022.101265

Lorius, C., Jouzel, J., Raynaud, D., Hansen, J., Treut, H.L., 1990. The ice-core record: climate sensitivity and future greenhouse warming. Nature 347, 139–145. https://doi.org/10.1038/347139a0

Murray, A., Arnold, L.J., Buylaert, J.-P., Guérin, G., Qin, J., Singhvi, A.K., Smedley, R., Thomsen, K.J., 2021. Optically stimulated luminescence dating using quartz. Nat Rev Methods Primers 1, 72. https://doi.org/10.1038/s43586-021-00068-5

Maher, B.A., 2016. Palaeoclimatic records of the loess/palaeosol sequences of the Chinese Loess Plateau. Quat. Sci. Rev. 154, 23–84. https://doi.org/10.1016/j.quascirev.2016.08.004

Negendank, J.F.W., Brauer, A., Zolitschka, B., 1990. Die Eifelmaare als erdgeschichtliche Fallen und Quellen zur Rekonstruktion des Paläoenvironments. Mainz. Geowiss. Mitt. 19, 235–262.

Paulick, H., Ewen, C., Blanchard, H., Zöller, L., 2009. The Middle-Pleistocene (~300 ka) Rodderberg maar-scoria cone volcanic complex (Bonn, Germany): eruptive history, geochemistry, and thermoluminescence dating. Int. J. Earth Sci. 98, 1879–1899. https://doi.org/10.1007/s00531-008-0341-0

Peng, J., Wang, X., Adamiec, G., 2022. The build-up of the laboratory-generated dose-response curve and underestimation of equivalent dose for quartz OSL in the high dose region: A critical modelling study. Quaternary Geochronology 67, 101231. https://doi.org/10.1016/j.quageo.2021.101231

Perić, Z., Lagerbäck Adolphi, E., Stevens, T., Újvári, G., Zeeden, C., Buylaert, J.-P., Marković, S.B., Hambach, U., Fischer, P., Schmidt, C., Schulte, P., Huayu, L., Shuangwen, Y., Lehmkuhl, F., Obreht, I., Veres, D., Thiel, C., Frechen, M., Jain, M., Vött, A., Zöller, L., Gavrilov, M.B., 2019. Quartz OSL dating of late quaternary Chinese and Serbian loess: A cross Eurasian comparison of dust mass accumulation rates. Quat. Int. 502, 30–44. https://doi.org/10.1016/j.quaint.2018.01.010

Perić, Z.M., Stevens, T., Obreht, I., Hambach, U., Lehmkuhl, F., Marković, S.B., 2022. Detailed luminescence dating of dust mass accumulation rates over the last two glacial-interglacial cycles from the Irig loess-palaeosol sequence, Carpathian Basin. Global and Planetary Change 215, 103895. https://doi.org/10.1016/j.gloplacha.2022.103895

Prescott, J.R., Hutton, J.T., 1994. Cosmic ray contributions to dose rates for luminescence and ESR dating: Large depths and long-term time variations. Radiat. Meas. 23, 497–500. https://doi.org/10.1016/1350-4487(94)90086-8

Qin, J., Chen, J., Li, Y., Zhou, L., 2018. Initial sensitivity change of K-feldspar pIRIR signals due to uncompensated decrease in electron trapping probability: Evidence from radiofluorescence measurements. Radiation Measurements 120, 131–136. https://doi.org/10.1016/j.radmeas.2018.06.017

Rees-Jones, J., Tite, M.S., 1997. OPTICAL DATING RESULTS FOR BRITISH ARCHAEOLOGICAL SEDIMENTS. Archaeometry 39, 177–187. https://doi.org/10.1111/j.1475-4754.1997.tb00797.x

Remy, H., 1960. Die zeitliche Stellung der Rodderbergtuffe im Rheinischen Löss. Decheniana 112, 271–278.

Richter, M., Tsukamoto, S., Long, H., 2020. ESR dating of Chinese loess using the quartz Ti centre: A comparison with independent age control. Quaternary International 556, 159–164. https://doi.org/10.1016/j.quaint.2019.04.003

Roberts, H.M., 2008. The development and application of luminescence dating to loess deposits: a perspective on the past, present and future. Boreas 37, 483–507. https://doi.org/10.1111/j.1502-3885.2008.00057.x

Römer, W., Lehmkuhl, F., Sirocko, F., 2016. Late Pleistocene aeolian dust provenances and wind direction changes reconstructed by heavy mineral analysis of the sediments of the Dehner dry maar (Eifel, Germany). Global and Planetary Change 147, 25–39. https://doi.org/10.1016/j.gloplacha.2016.10.012

Seelos, K., Sirocko, F., Dietrich, S., 2009. A continuous high-resolution dust record for the reconstruction of wind systems in central Europe (Eifel, Western Germany) over the past 133 ka. Geophys. Res. Lett. 36, L20712. https://doi.org/10.1029/2009GL039716

Schläfli, P., Gobet, E., Hogrefe, I., Bittmann, F., Schlunegger, F., Zolitschka, B., Tinner, W., 2023. New vegetation history reconstructions suggest a biostratigraphic assignment of the lowermost Rodderberg interglacial (Germany) to MIS 11. Quat. Sci. Rev. 302, 107932. https://doi.org/10.1016/j.quascirev.2022.107932

Schmidt, C., Bösken, J., Kolb, T., 2018. Is there a common alpha-efficiency in polymineral samples measured by various infrared stimulated luminescence protocols? Geochronometria 45, 160–172. https://doi.org/10.1515/geochr-2015-0095

Schmidt, E.D., Frechen, M., Murray, A.S., Tsukamoto, S., Bittmann, F., 2011a. Luminescence chronology of the loess record from the Tönchesberg section: A comparison of using quartz and feldspar as dosimeter to extend the age range beyond the Eemian. Quat. Int. 234, 10–22. https://doi.org/10.1016/j.quaint.2010.07.012

Schmidt, E.D., Semmel, A., Frechen, M., 2011b. Luminescence dating of the loess/palaeosol sequence at the gravel quarry Gaul/Weilbach, Southern Hesse (Germany). E&G Quat. Sci. J. 60, 116–125. https://doi.org/10.3285/eg.60.1.08

Schmidt, E.D., Tsukamoto, S., Frechen, M., Murray, A.S., 2014. Elevated temperature IRSL dating of loess sections in the East Eifel region of Germany. Quat. Int. 334–335, 141–154. https://doi.org/10.1016/j.quaint.2014.03.006

Schmincke, H., 2007. The Quaternary Volcanic Fields of the East and West Eifel (Germany). In: Ritter, J.R.R., Christensen, U.R. (eds) Mantle Plumes. Springer, Berlin, Heidelberg. https://doi.org/10.1007/978-3-540-68046-8_8

Sirocko, F., Knapp, H., Dreher, F., Förster, M.W., Albert, J., Brunck, H., Veres, D., Dietrich, S., Zech, M., Hambach, U., Röhner, M., Rudert, S., Schwibus, K., Adams, C., Sigl, P., 2016. The ELSA-Vegetation-Stack: Reconstruction of Landscape Evolution Zones (LEZ) from laminated Eifel maar sediments of the last 60,000 years. Global and Planetary Change 142, 108–135. https://doi.org/10.1016/j.gloplacha.2016.03.005

Sirocko, F., Seelos, K., Schaber, K., Rein, B., Dreher, F., Diehl, M., Lehne, R., Jäger, K., Krbetschek, M., Degering, D., 2005. A late Eemian aridity pulse in central Europe during the last glacial inception. Nature 436, 833–836. https://doi.org/10.1038/nature03905

Sohbati, R., Murray, A.S., Buylaert, J.-P., Ortuño, M., Cunha, P.P., Masana, E., 2012. Luminescence dating of Pleistocene alluvial sediments affected by the Alhama de Murcia fault (eastern Betics, Spain) - a comparison between OSL, IRSL and post-IRIRSL ages: Luminescence dating of Pleistocene alluvial sediments. Boreas 41, 250–262. https://doi.org/10.1111/j.1502-3885.2011.00230.x

Steup, R., Fuchs, M., 2017. The loess sequence at Münzenberg (Wetterau/Germany): A reinterpretation based on new luminescence dating results. Z. Für Geomorphol. Suppl. Issues. https://doi.org/10.1127/zfg_suppl/2017/0408

Svendsen, J.I., Alexanderson, H., Astakhov, V.I., Demidov, I., Dowdeswell, J.A., Funder, S., Gataullin, V., Henriksen, M., Hjort, C., Houmark-Nielsen, M., Hubberten, H.W., Ingolfsson, O., Jakobsson, M., Kjaer, K.H., Larsen, E., Lokrantz, H., Lunkka, J.P., Lysa, A., Mangerud, J., Matiouchkov, A., Murray, A., Moller, P., Niessen, F., Nikolskaya, O., Polyak, L., Saarnisto, M., Siegert, C., Siegert, M.J., Spielhagen, R.F., Stein, R., 2004. Late quaternary ice sheet history of northern Eurasia. Quat. Sci. Rev. 23, 1229–1271.

Thiel, C., Buylaert, J.-P., Murray, A., Terhorst, B., Hofer, I., Tsukamoto, S., Frechen, M., 2011. Luminescence dating of the Stratzing loess profile (Austria) – Testing the potential of an elevated temperature post-IR IRSL protocol. Quat. Int. 234, 23–31. https://doi.org/10.1016/j.quaint.2010.05.018

Thiel, C., Horváth, E., Frechen, M., 2014. Revisiting the loess/palaeosol sequence in Paks, Hungary: A post-IR IRSL based chronology for the 'Young Loess Series.' Quat. Int. 319, 88–98. https://doi.org/10.1016/j.quaint.2013.05.045

Thomsen, K.J., Murray, A.S., Jain, M., Bøtter-Jensen, L., 2008. Laboratory fading rates of various luminescence signals from feldspar-rich sediment extracts. Radiat. Meas. 43, 1474–1486. https://doi.org/10.1016/j.radmeas.2008.06.002

Timar-Gabor, A., Buylaert, J.P., Guralnik, B., Trandafir-Antohi, O., Constantin, D., Anechitei-Deacu, V., Jain, M., Murray, A.S., Porat, N., Hao, Q., Wintle, A.G., 2017. On the importance of grain size in luminescence dating using quartz. Radiat. Meas. 106, 464–471. https://doi.org/10.1016/j.radmeas.2017.01.009

Timar-Gabor, A., Constantin, D., Buylaert, J.P., Jain, M., Murray, A.S., Wintle, A.G., 2015. Fundamental investigations of natural and laboratory generated SAR dose response curves for quartz OSL in the high dose range. Radiat. Meas. 81, 150–156. https://doi.org/10.1016/j.radmeas.2015.01.013

Timar-Gabor, A., Vandenberghe, D.A.G., Vasiliniuc, S., Panaoitu, C.E., Panaiotu, C.G., Dimofte, D., Cosma, C., 2011. Optical dating of Romanian loess: A comparison between silt-sized and sand-sized quartz. Quat. Int. 240, 62–70. https://doi.org/10.1016/j.quaint.2010.10.007

Timar-Gabor, A., Wintle, A.G., 2013. On natural and laboratory generated dose response curves for quartz of different grain sizes from Romanian loess. Quat. Geochronol. 18, 34–40. https://doi.org/10.1016/j.quageo.2013.08.001

Wacha, L., Vlahović, I., Tsukamoto, S., Kovačić, M., Hasan, O., Pavelić, D., 2016. The chronostratigraphy of the latest Middle Pleistocene aeolian and alluvial activity on the Island of Hvar, eastern Adriatic, Croatia. Boreas 45, 152–164. https://doi.org/10.1111/bor.12141

Wang, X., Peng, J., Adamiec, G., 2021. Extending the age limit of quartz OSL dating of Chinese loess using a new multiple-aliquot regenerative-dose (MAR) protocol with carefully selected preheat conditions. Quaternary Geochronology 62, 101144. https://doi.org/10.1016/j.quageo.2020.101144

Wintle, A.G., 1973. Anomalous Fading of Thermo-luminescence in Mineral Samples. Nature 245, 143–144. https://doi.org/10.1038/245143a0

Wintle, A.G., Murray, A.S., 2006. A review of quartz optically stimulated luminescence characteristics and their relevance in single-aliquot regeneration dating protocols. Radiat. Meas. 41, 369–391. https://doi.org/10.1016/j.radmeas.2005.11.001

Yi, S., Buylaert, J.-P., Murray, A.S., Lu, H., Thiel, C., Zeng, L., 2016. A detailed post-IR IRSL dating study of the Niuyangzigou loess site in northeastern China. Boreas 45, 644–657. https://doi.org/10.1111/bor.12185

Zens, J., Schulte, P., Klasen, N., Krauß, L., Pirson, S., Burow, C., Brill, D., Eckmeier, E., Kels, H., Zeeden, C., Spagna, P., Lehmkuhl, F., 2018. OSL chronologies of paleoenvironmental dynamics recorded by loess-paleosol sequences from Europe: Case studies from the Rhine-Meuse area and the Neckar Basin. Palaeogeogr. Palaeoclimatol. Palaeoecol. 509, 105–125. https://doi.org/10.1016/j.palaeo.2017.07.019

Zhang, J., 2018. Behavior of the electron trapping probability change in IRSL dating of K-feldspar: A dose recovery study. Quat. Geochronol. 44, 38–46. https://doi.org/10.1016/j.quageo.2017.12.001

Zhang, J., Hao, Q., Li, S.-H., 2022. An absolutely dated record of climate change over the last three glacial–interglacial cycles from Chinese loess deposits. Geology 50, 1116–1120. https://doi.org/10.1130/G50125.1

Zolitschka, B., Brauer, A., Negendank, J.F.W., Stockhausen, H., Lang, A., 2000. Annually dated late Weichselian continental paleoclimate record from the Eifel, Germany. Geol 28, 783. https://doi.org/10.1130/0091-7613(2000)28<783:ADLWCP>2.0.CO;2

Zolitschka, B., Rolf, C., Bittmann, F., Binot, F., Frechen, M., Wonik, T., Froitzheim, N., Ohlendorf, C., 2014. Pleistocene climatic and environmental variations inferred from a terrestrial sediment record – the Rodderberg Volcanic Complex near Bonn, Germany. Z. Dtsch. Ges. Für Geowiss. 165, 407–424. https://doi.org/10.1127/1860-1804/2014/0071

Zöller, L., Blanchard, H., 2009. The partial heat – longest plateau technique: Testing TL dating of Middle and Upper Quaternary volcanic eruptions in the Eifel Area, Germany. EampG Quat. Sci. J. 58, 86–106. https://doi.org/10.3285/eg.58.1.05

Zöller, L., Hambach, U., Blanchard, H., Fischer, S., Köhne, S., Stritzke, R., 2010. Der Rodderberg-Krater bei Bonn : Ein komplexes Geoarchiv. EampG Quat. Sci. J. 59, 44–58. https://doi.org/10.3285/eg.59.1-2.04

Tables

Table 1. Quartz OSL protocol and three pIRIR protocols of the polymineral fraction used in this study. Note that some samples are also measured without hot-bleach in Step 9 for the $pIRIR_{225}$ protocol.

Step	Quartz OSL	$pIRIR_{225}$	pulsed $pIRIR_{150}$	MET-$pIRIR_{250}$
1	Give dose, D_i	Give dose, D_i	Give dose, D_i	Give dose, D_i
2	Preheat at 220 °C for 10 s	Preheat at 250 °C for 60 s	Preheat at 250 °C for 60 s	Preheat at 300 °C for 60 s
3	OSL for 40 s at 125 °C (L_x)	IRSL for 100 s at 50 °C	IRSL for 100 s at 50 °C	IRSL for 100 s at 50 °C
4	Test dose, D_t	IRSL for 200 s at 225 °C (L_x)	Pulsed IRSL for 500 s at 150 °C (L_x)	IRSL for 100 s at 100 °C
5	Cutheat to 200 °C	Test dose, D_t	Test dose, D_t	IRSL for 100 s at 150 °C
6	OSL for 40 s at 125 °C (T_x)	Preheat at 250 °C for 60 s	Preheat at 250 °C for 60 s	IRSL for 100 s at 200 °C
7	Return to step 1	IRSL for 100 s at 50 °C	IRSL for 100 s at 50 °C	IRSL for 100 s at 250 °C (L_x)
8		IRSL for 200 s at 225 °C (T_x)	Pulsed IRSL for 500 s at 150 °C (T_x)	Test dose, D_t
9		IR bleach at 290 °C for 40 s	IR bleach at 200 °C for 100 s	Preheat at 300 °C for 60 s
10		Return to step 1	Return to step 1	IRSL for 100 s at 50 °C
11				IRSL for 100 s at 100 °C
12				IRSL for 100 s at 150 °C
13				IRSL for 100 s at 200 °C
14				IRSL for 100 s at 250 °C (T_x)
15				IR bleach at 320 °C for 100 s
16				Return to step 1

Table 2. Summary of U, Th and K concentrations, $^{210}Pb/^{214}Pb$ activity ratio and dose rates for fine-grained quartz and polymineral fractions. For the first sample (LUM4606), 25 % Rn loss is assumed for dose rate calculation. For other samples, no Rn loss is assumed. A constant water content error of 5 % is used for all samples.

Sample	Composite depth (m)	Water (%)	U (ppm)		Th (ppm)		K (%)		Pb^{210}/Pb^{214}	Dose rate (Gy/ka)			
			mean ± err		mean ± err		mean ± err			Polymineral		Quartz	
4606	0.50	30.5	3.77	0.19	13.97	0.70	2.05	0.10	0.75	4.00	0.19	3.50	0.14
4629	1.00	23.6	3.40	0.17	12.56	0.63	1.84	0.09	0.95	4.02	0.20	3.49	0.15
4371	1.73	22.1	2.84	0.15	12.13	0.61	1.90	0.10	1.08	3.88	0.19	3.39	0.14
4607	2.50	19.7	3.51	0.18	13.22	0.67	1.77	0.09	0.99	4.17	0.22	3.60	0.16
4631	3.00	18.2	3.38	0.17	13.00	0.65	1.75	0.09	0.98	4.15	0.22	3.58	0.16
4632	3.40	17.8	3.14	0.16	12.74	0.64	1.84	0.09	1.02	4.12	0.21	3.58	0.16
4608	3.80	15.3	3.11	0.16	12.44	0.63	2.03	0.10	0.96	4.35	0.22	3.79	0.17
4374	4.80	18.6	3.07	0.16	12.60	0.63	1.95	0.10	0.94	4.16	0.21	3.62	0.16
4451	5.00	18.6	2.97	0.15	11.88	0.60	1.93	0.10	1.08	4.00	0.20	3.49	0.15
4452	5.40	20.0	2.85	0.15	11.36	0.57	1.89	0.10	1.05	3.82	0.19	3.33	0.15
4609	6.20	23.1	3.12	0.16	12.26	0.62	1.90	0.10	1.02	3.88	0.20	3.37	0.14
4610	7.10	25.6	3.46	0.18	13.03	0.66	1.83	0.09	0.91	3.90	0.20	3.37	0.14
4633	7.71	20.0	3.25	0.17	12.80	0.65	1.88	0.10	0.95	4.06	0.21	3.52	0.15
4634	7.94	22.4	3.04	0.15	11.76	0.59	1.96	0.10	0.92	3.86	0.19	3.37	0.15
4635	8.30	22.1	3.25	0.17	11.81	0.59	1.79	0.09	0.99	3.80	0.20	3.29	0.14
4636	8.30	35.5	2.97	0.15	12.11	0.61	1.85	0.09	1.10	3.36	0.16	2.92	0.12
4611	8.70	32.5	3.07	0.16	12.46	0.63	1.91	0.10	1.03	3.55	0.17	3.09	0.13
4453	9.30	22.1	3.18	0.16	11.66	0.59	1.75	0.09	0.98	3.73	0.19	3.22	0.14
4367	10.40	21.3	2.57	0.13	9.65	0.49	1.62	0.08	0.96	3.24	0.16	2.82	0.12
4454	12.10	25.1	2.71	0.14	10.50	0.53	1.64	0.08	1.15	3.25	0.16	2.82	0.12
4377	14.35	21.0	2.60	0.13	10.01	0.51	1.65	0.08	0.95	3.30	0.17	2.87	0.13
4372	18.50	30.9	2.80	0.14	10.47	0.53	1.54	0.08	1.07	3.01	0.15	2.60	0.11
4455	23.12	35.0	6.77	0.34	12.92	0.65	1.69	0.09	1.21	4.37	0.25	3.69	0.16
4370	26.46	24.0	2.51	0.13	9.43	0.48	1.75	0.09	0.85	3.18	0.16	2.78	0.12
4456	29.90	34.0	2.38	0.12	9.94	0.50	1.53	0.08	1.12	2.74	0.14	2.38	0.10
4457	31.32	34.4	2.63	0.14	10.87	0.55	1.62	0.08	1.04	2.95	0.15	2.55	0.11
4375	33.00	29.8	2.48	0.13	10.06	0.51	1.56	0.08	0.96	2.91	0.15	2.52	0.11
4458	34.82	54.1	2.09	0.11	7.84	0.40	1.20	0.06	1.03	1.90	0.09	1.63	0.06
4637	36.00	41.8	2.24	0.11	8.05	0.41	1.24	0.06	0.99	2.17	0.11	1.87	0.08
4369	37.54	26.9	2.71	0.14	9.79	0.50	1.56	0.08	1.00	3.03	0.15	2.62	0.11
4459	39.38	25.1	2.76	0.14	10.56	0.53	1.60	0.08	0.99	3.20	0.16	2.77	0.12
4460	42.39	30.6	2.54	0.13	10.79	0.54	1.80	0.09	1.02	3.15	0.16	2.74	0.12
4373	47.00	25.1	2.79	0.14	9.92	0.50	1.80	0.09	0.87	3.31	0.17	2.88	0.13
4381	50.82	23.7	2.91	0.15	10.32	0.52	1.81	0.09	0.98	3.44	0.17	2.99	0.13
4368	60.00	28.3	3.00	0.16	11.64	0.59	1.74	0.09	0.98	3.38	0.17	2.92	0.13

4379	64.00	42.9	2.75	0.14	10.61	0.53	1.55	0.08	0.95	2.70	0.13	2.33	0.09
4376	65.00	42.6	2.84	0.15	12.10	0.61	2.04	0.10	0.91	3.19	0.15	2.79	0.11
4382	68.91	62.5	2.57	0.13	10.45	0.53	1.82	0.09	1.02	2.44	0.11	2.13	0.08
4378	69.98	24.9	3.17	0.16	10.81	0.54	2.09	0.10	0.95	3.75	0.19	3.28	0.14
4365	72.04	24.0	2.78	0.14	12.83	0.65	2.70	0.14	0.92	4.34	0.21	3.85	0.17

Table 3. Ages of fine-grained polymineral (MET-pIRIR$_{250}$) and fine-grained quartz (OSL). The error (err) provided is 1 sigma. For D_e values of the MET-pIRIR$_{250}$ signal a constant residual dose of 5.2 Gy is already subtracted.

LUM number	Sample ID	Composite depth (m)	D_e (Gy)	err	Dose rate (Gy/ka)	err	Age (ka)	err
4–11 µm polymineral, MET-pIRIR$_{250}$								
4606	ROD11-2-1-1_50cm	0.50	10.3	0.2	4.00	0.19	2.6	0.1
4629	ROD11-2-1-2_25cm	1.00	73	2	4.02	0.20	18.3	1.1
4371	ROD11-3-1-2_50cm	1.73	80	2	3.88	0.19	20.5	1.1
4607	ROD11-2-1-3_80cm	2.50	138	3	4.17	0.22	33.0	1.8
4631	ROD11-2-2-1_25cm	3.00	186	6	4.15	0.22	44.9	2.8
4632	ROD11-2-2-1_65cm	3.40	300	8	4.12	0.21	72.9	4.2
4608	ROD11-2-2-2_20cm	3.80	502	16	4.35	0.22	116	7
4374	ROD11-3-2-3_40cm	4.80	532	25	4.16	0.21	128	9
4451	ROD11-3-2-3_60cm	5.00	514	12	4.00	0.20	128	7
4452	ROD11-3-3-1_30cm	5.40	504	25	3.82	0.19	132	9
4609	ROD11-3-4-1_60cm	6.20	562	21	3.88	0.20	145	9
4610	ROD11-3-4-2_50cm	7.10	495	21	3.90	0.20	127	8
4633	ROD11-2-4-1_39cm	7.71	514	17	4.06	0.21	127	8
4634	ROD11-2-4-1_62cm	7.94	503	33	3.86	0.19	130	11
4635	ROD11-2-4-2_15cm	8.30	458	17	3.80	0.20	120	8
4636	ROD11-3-5-1_40cm	8.30	475	16	3.36	0.16	142	8
4611	ROD11-3-5-1_80cm	8.70	449	12	3.55	0.17	126	7
4453	ROD11-3-5-2_20cm	9.30	441	7	3.73	0.19	119	6
4367	ROD11-3-5-3_20cm	10.40	450	9	3.24	0.16	139	8
4454	ROD11-3-6-2_20cm	12.10	476	11	3.25	0.16	146	8
4377	ROD11-3-7-1_70cm	14.35	528	17	3.30	0.17	160	10
4372	ROD11-3-8-2_70cm	18.50	473	12	3.01	0.15	157	9
4455	ROD11-3-10-1_20cm	23.12	785	22	4.37	0.25	179	11
4370	ROD11-3-11-1_50cm	26.46	665	19	3.18	0.16	209	12
4456	ROD11-3-12-2_30cm	29.90	600	28	2.74	0.14	219	15
4457	ROD11-3-12-3_80cm	31.32	639	13	2.95	0.15	216	12
4375	ROD11-3-13_50cm	33.00	638	16	2.91	0.15	219	12
4458	ROD11-3-14-3_20cm	34.92	505	14	1.90	0.09	266	15
4637	ROD11-3-15-1_30cm	36.00	548	19	2.17	0.11	252	15
4369	ROD11-3-15-2_80cm	37.54	742	47	3.03	0.15	245	20
4459	ROD11-3-16-2_65cm	39.38	669	7	3.20	0.16	209	11
4460	ROD11-3-17-3-30cm	42.39	690	12	3.15	0.16	219	11
4373	ROD11-3-20-2_30cm	47.00	782	17	3.31	0.17	237	13
4381	ROD11-3-21-2_60cm	50.82	786	42	3.44	0.17	229	17
4368	ROD11-3-24-3_50cm	58.00	871	65	3.38	0.17	257	23
4379	ROD11-3-25-3_20cm	60.00	697	47	2.70	0.13	258	22

4376	ROD11-3-26-2_50cm	64.00	837	40	3.19	0.15	263	18
4382	ROD11-3-27-3 (b)_53cm	68.91	775	50	2.44	0.11	318	25
4378	ROD11-3-28-1_60cm	69.98	962	54	3.75	0.19	256	19
4365	ROD11-3-28-3_70cm	72.04	1161	78	4.34	0.21	267	22
4–11 µm quartz, OSL								
4606	ROD11-2-1-1_50cm	0.50	3.18	0.04	3.50	0.14	0.91	0.04
4629	ROD11-2-1-2_25cm	1.00	46.0	0.3	3.49	0.15	13.2	0.6
4371	ROD11-3-1-2_50cm	1.73	57.1	0.8	3.39	0.14	16.8	0.8
4607	ROD11-2-1-3_80cm	2.50	108	3	3.60	0.16	30.0	1.5
4631	ROD11-2-2-1_25cm	3.00	156	1	3.58	0.16	43.7	1.9
4632	ROD11-2-2-1_65cm	3.40	218	4	3.58	0.16	60.8	2.9
4608	ROD11-2-2-2_20cm	3.80	298	11	3.79	0.17	78.4	4.6
4374	ROD11-3-2-3_40cm	4.80	341	12	3.62	0.16	94.1	5.3
4451	ROD11-3-2-3_60cm	5.00	352	4	3.49	0.15	100.8	4.6
4452	ROD11-3-3-1_30cm	5.40	316	3	3.33	0.15	94.8	4.2
4609	ROD11-3-4-1_60cm	6.20	312	4	3.37	0.14	92.6	4.2
4610	ROD11-3-4-2_50cm	7.10	340	9	3.37	0.14	101.0	5.0
4453	ROD11-3-5-2_20cm	9.30	329	5	3.22	0.14	102.0	4.7
4367	ROD11-3-5-3_20cm	10.40	312	6	2.82	0.12	110.8	5.3
4454	ROD11-3-6-2_20cm	12.10	326	3	2.82	0.12	115.5	5.1
4377	ROD11-3-7-1_70cm	14.35	328	5	2.87	0.13	114.3	5.3
4372	ROD11-3-8-2_70cm	18.50	323	1	2.60	0.11	124.3	5.3
4455	ROD11-3-10-1_20cm	23.12	436	2	3.69	0.16	118.3	5.2
4456	ROD11-3-12-2_30cm	29.90	357	5	2.38	0.10	150.4	6.6

Table 4. Fading corrected ages of the $pIRIR_{225}$ signal and the pulsed $pIRIR_{150}$ signal of polymineral fine grains (4–11 µm). For samples with apparent ages < 50 ka, the fading correction of Huntley and Lamothe (2001) is applied. For samples with apparent ages > 50 ka, the fading correction of Kars et al. (2008) is applied.

LUM	Depth (m)	Dose rate (Gy/ka)		D_e (Gy)		g_{2d} (%)		Apparent age (ka)		Corrected age (ka)		$2D_0$ age (ka)
$pIRIR_{225}$		mean	err	mean	err	mean	err	mean	err	mean	err	
4629	1.00	4.02	0.20	46.9	0.3	1.63	0.69	11.7	0.6	13.5	1.1	
4371	1.73	3.88	0.19	66.6	0.3	1.30	0.35	17.2	0.9	19.2	1.2	
4607	2.50	4.17	0.22	117	3	1.21	0.44	28.0	1.6	30.8	1.9	
4631	3.00	4.15	0.22	166	2	1.30	0.38	40.1	2.1	45.0	3.0	
4632	3.40	4.12	0.21	242	6	1.34	0.58	58.7	3.4	75.0	5.5	
4608	3.80	4.35	0.22	403	3	1.23	0.49	93	5	117	7	
4452	5.40	3.82	0.19	398	9	1.29	0.33	104	6	138	8	
4609	6.20	3.88	0.20	430	9	1.41	0.55	111	6	150	9	
4610	7.10	3.90	0.20	427	7	1.13	0.54	110	6	140	8	
4453	9.30	3.73	0.19	378	8	1.21	0.52	101	6	132	8	
4367	10.37	3.24	0.16	364	9	1.15	0.39	112	7	142	8	275±15
4454	12.10	3.25	0.16	366	9	0.96	0.54	113	6	137	8	262±15
4377	14.35	3.30	0.17	378	7	1.15	0.56	114	6	144	9	270±16
4372	18.50	3.01	0.15	383	10	1.48	0.53	127	7	169	14	290±17
4455	23.12	4.37	0.25	608	8	1.25	0.67	139	8	181	13	193±13
4370	26.46	3.18	0.16	594	17	1.27	0.43	187	11	274	18	269±17[#]
4370*				546	11	1.33	0.60	172	9	249	15	260±15
4456	29.90	2.74	0.14	457	8	1.04	0.58	166	9	213	13	297±18
4457	31.32	2.95	0.15	510	12	0.99	0.56	173	10	223	13	281±18
4375	33.00	2.91	0.15	532	12	1.38	0.58	183	10	266	17	286±17
4375*				479	10	1.38	0.58	165	9	230	15	287±17
4458	34.92	1.90	0.09	364	20	1.29	0.61	192	14	253	20	455±26
4637	36.00	2.17	0.11	392	20	1.57	0.59	180	13	259	21	390±23
4369	37.54	3.03	0.15	520	31	1.44	0.58	172	13	258	27	275±16
4459	39.38	3.20	0.16	576	35	1.36	0.46	180	14	265	28	293±16
4460	42.39	3.15	0.16	551	11	1.01	0.56	175	9	234	20	254±16
4373	47.00	3.31	0.17	560	42	1.42	0.54	169	15	321	39	287±16[#]
4368	58.00	3.38	0.17	666	50	1.44	0.49	197	18	326	41	274±15[#]
4378	69.98	3.75	0.19	838	78	1.70	0.58	223	24	774	144	265±15[#]
Pulsed $pIRIR_{150}$												
4371	1.73	3.88	0.19	66.1	0.7	1.03	0.67	17.0	0.9	18.5	1.4	
4374	4.80	4.16	0.21	448	5	0.95	0.72	108	6	131	8	178±10
4367	10.40	3.24	0.16	393	4	0.16	0.74	121	6	137	8	229±13
4377	14.35	3.30	0.17	389	5	1.51	0.86	118	6	162	10	219±13
4372	18.50	3.01	0.15	389	4	1.06	0.92	129	7	155	9	237±14

*samples are measured without hot-bleach at the end of each cycle (step 9 for the $pIRIR_{225}$ protocol in Table 1).

#when the fading corrected age is larger than the $2D_0$ age, this fading corrected age is not reliable. Empirically, the $2D_0$ age can be regarded as the minimum age.

Table 5. The electron trap (E) and frequency factor (*s*) of each aliquot deduced from isothermal annealing. For samples with two aliquots measured, the mean E value is an arithmetic mean, and the mean *s* is a geometric mean. Lifetime at 20 °C (τ_{20}) is calculated from the equation: $\tau = (1/s)*e^{E/kT}$.

Sample origin	ID	Aliquot	E (eV)	*s* (s^{-1})	τ_{20} (Ma)
Rodderberg loess (4–11 μm)	LUM4608	1	1.737	3.93E+14	57
		2	1.751	7.54E+14	52
		Mean	1.744	5.45E+14	54
	LUM4632	1	1.793	1.51E+15	137
		2	1.712	2.20E+14	38
		Mean	1.753	5.77E+14	73
Risø calibration quartz (180–250 μm)	Batch60	1	1.759	5.45E+14	97
	Batch200	1	1.788	1.47E+15	114
		2	1.774	1.02E+15	96
		Mean	1.781	1.23E+15	105

Figures

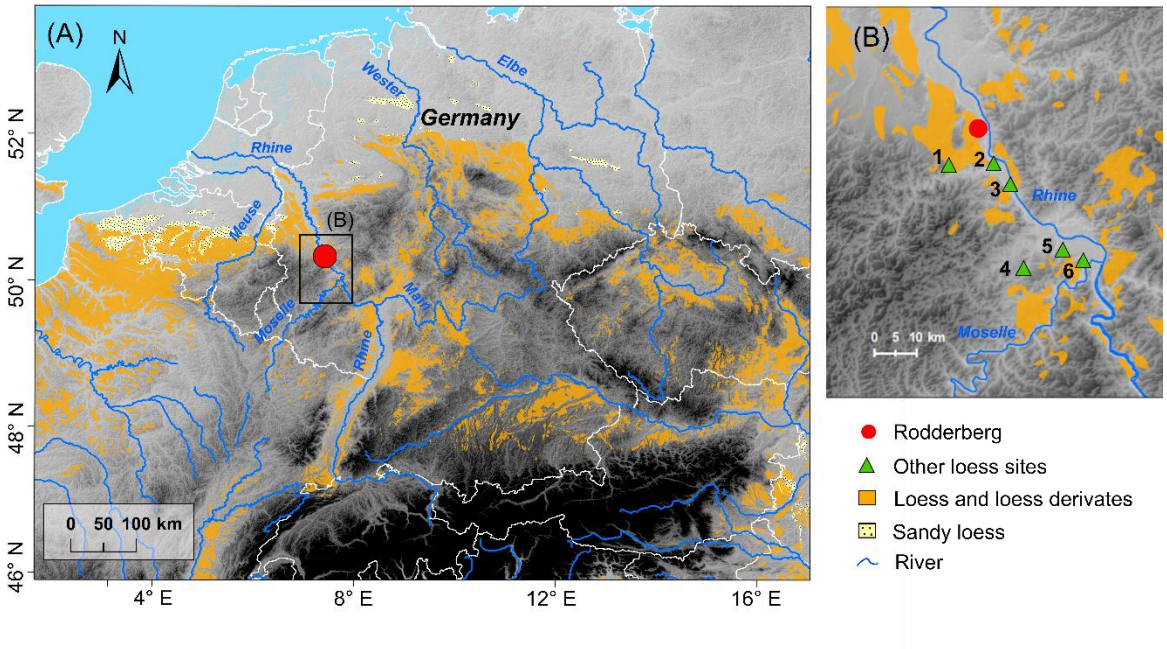

Fig 1. Location of Rodderberg in Germany (A) and in the Middle Rhine Valley (B) together with other regional and well-studied loess-paleosol sequences mentioned in the text. 1 – Ringen, 2 – Schwalbenberg, 3 – Ariendorf, 4 – Tönchesberg, 5 – Kärlich, 6 – Koblenz-Metternich. The loess distribution for Central Europe is modified from Lehmkuhl et al. (2018).

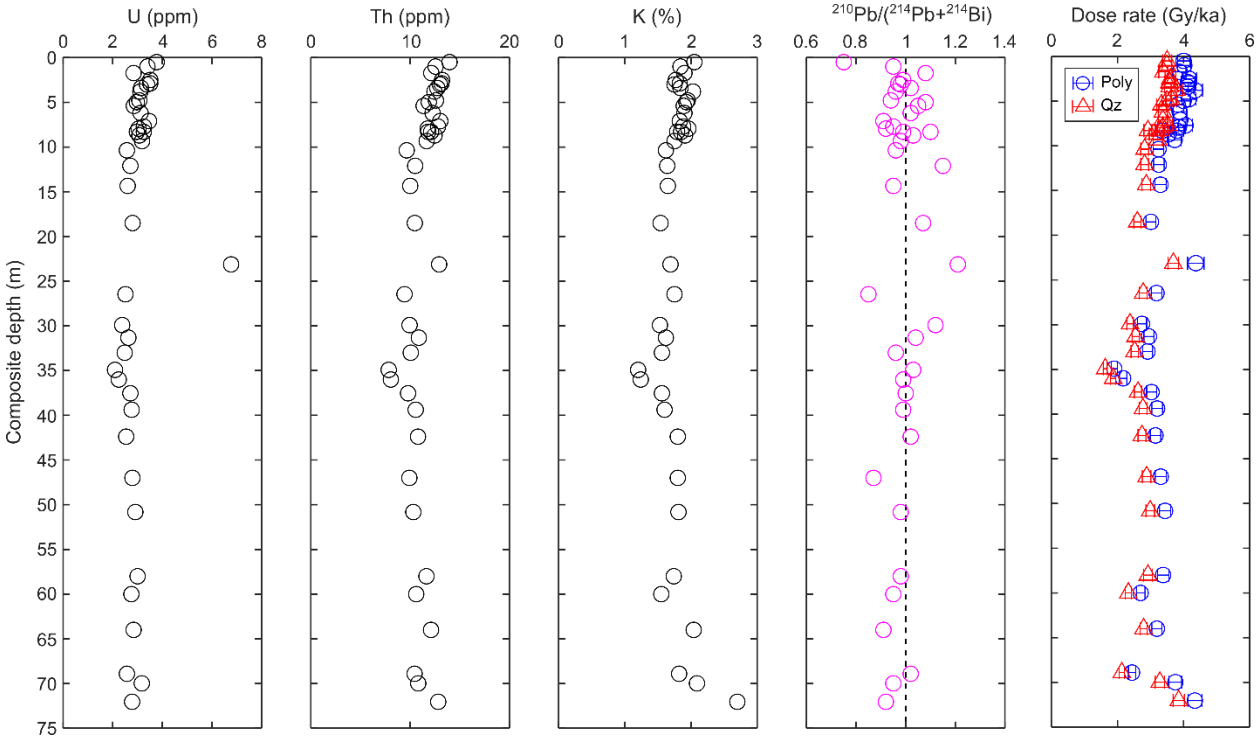

Fig. 2. U, Th and K concentrations, ratio of activity of ^{210}Pb to the mean activity of (^{214}Pb+^{214}Bi) and dose rates of the fine-grained polymineral and quartz fractions.

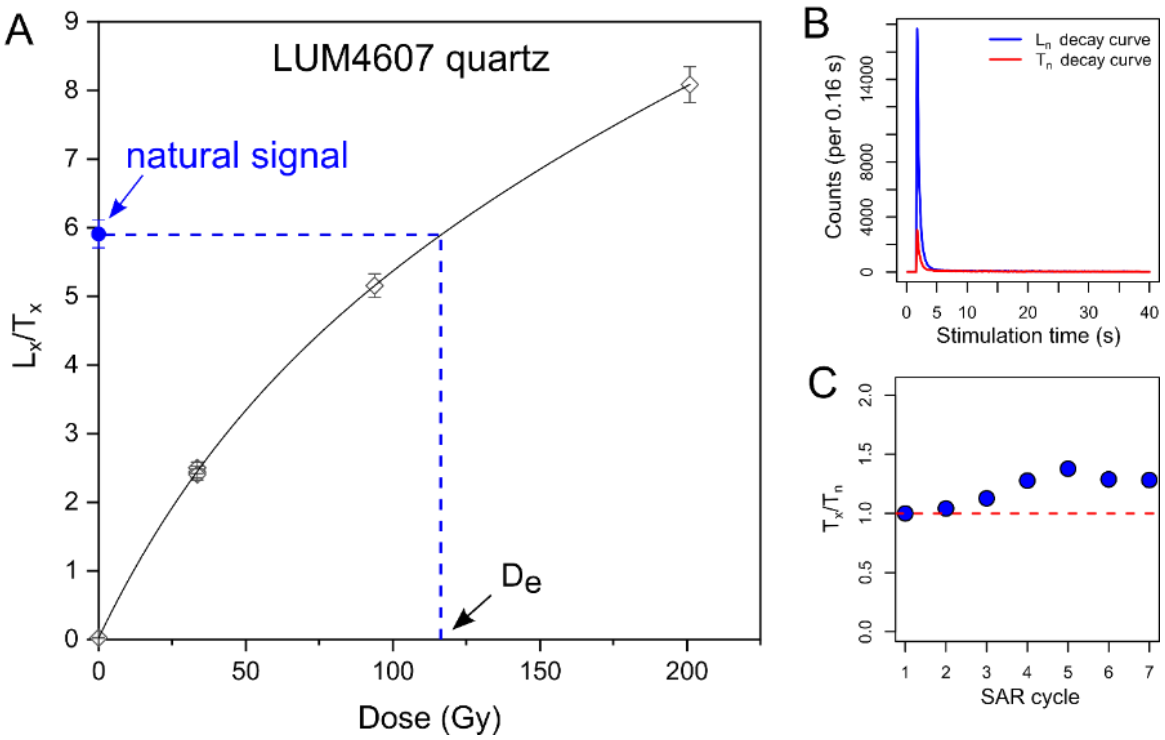

Fig. 3. A) Dose-response curve and D_e estimation of the OSL signal from a fine-grained quartz aliquot of sample LUM4607. B) Natural signal and test dose (14 Gy) signal. C) Sensitivity change of the OSL signal within the SAR protocol.

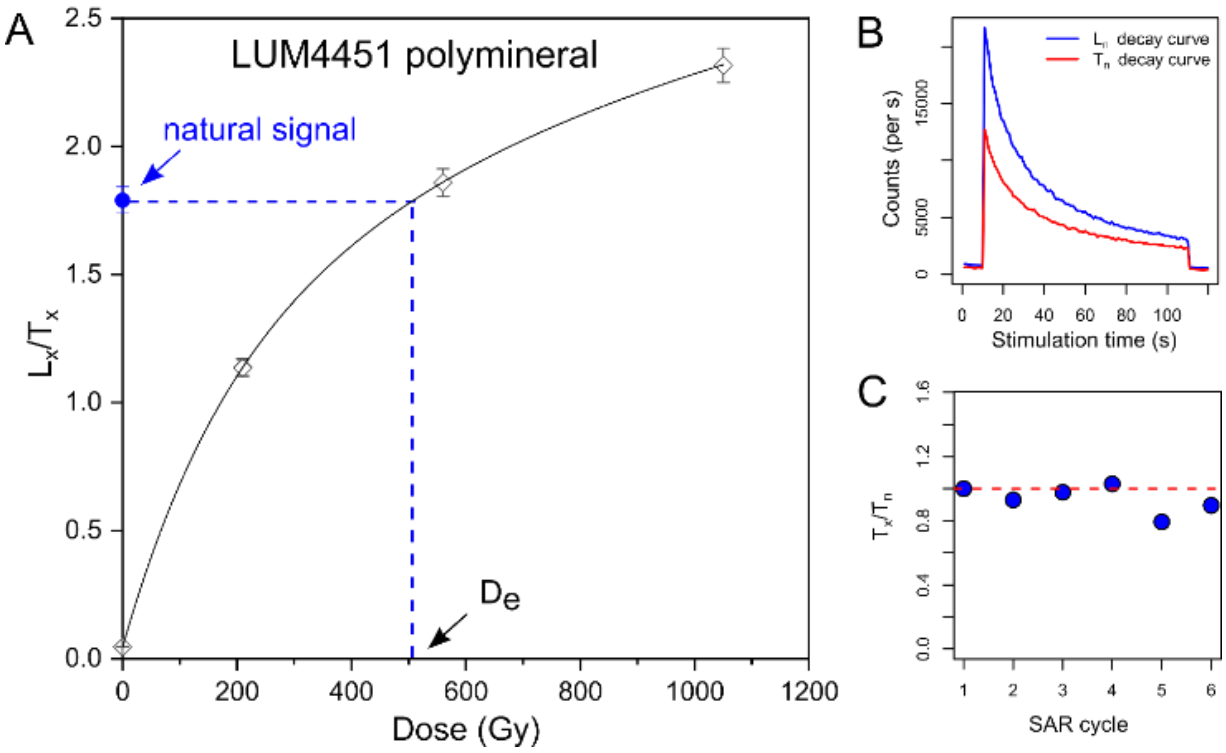

Fig. 4. A) Dose-response curve and D_e estimation for the MET-pIRIR$_{250}$ signal from a fine-grained polymineral aliquot of sample LUM4451. B) Natural signal and test dose (140 Gy) signal of MET-pIRIR$_{250}$. C) Sensitivity change of the MET-pIRIR$_{250}$ signal within the SAR protocol.

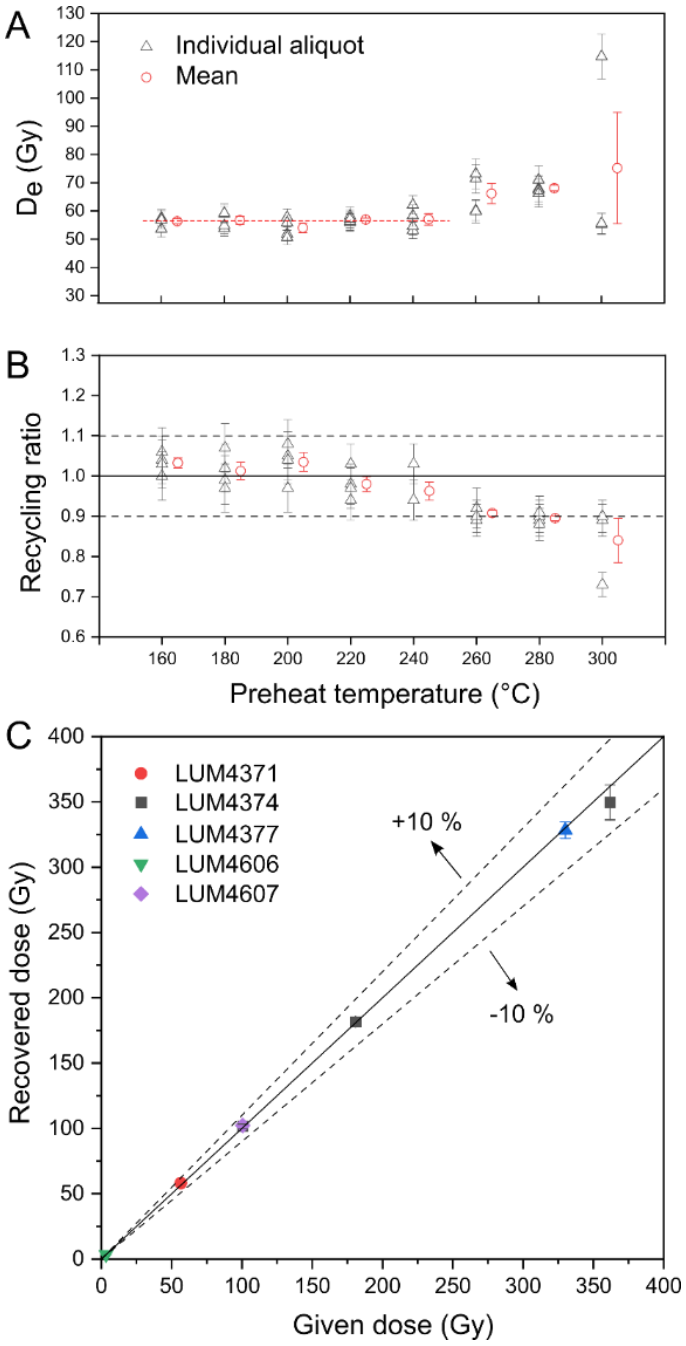

Fig. 5. Luminescence characteristics of the fine-grained quartz OSL signal. A) D_e values with different preheat temperatures. Stable D_e is obtained within the preheat temperature range of 160-240 °C. B) Recycling ratios with different preheat temperatures. C) Dose recovery tests with a preheat temperature of 220 °C. The recovered doses are within 10 % of the given doses.

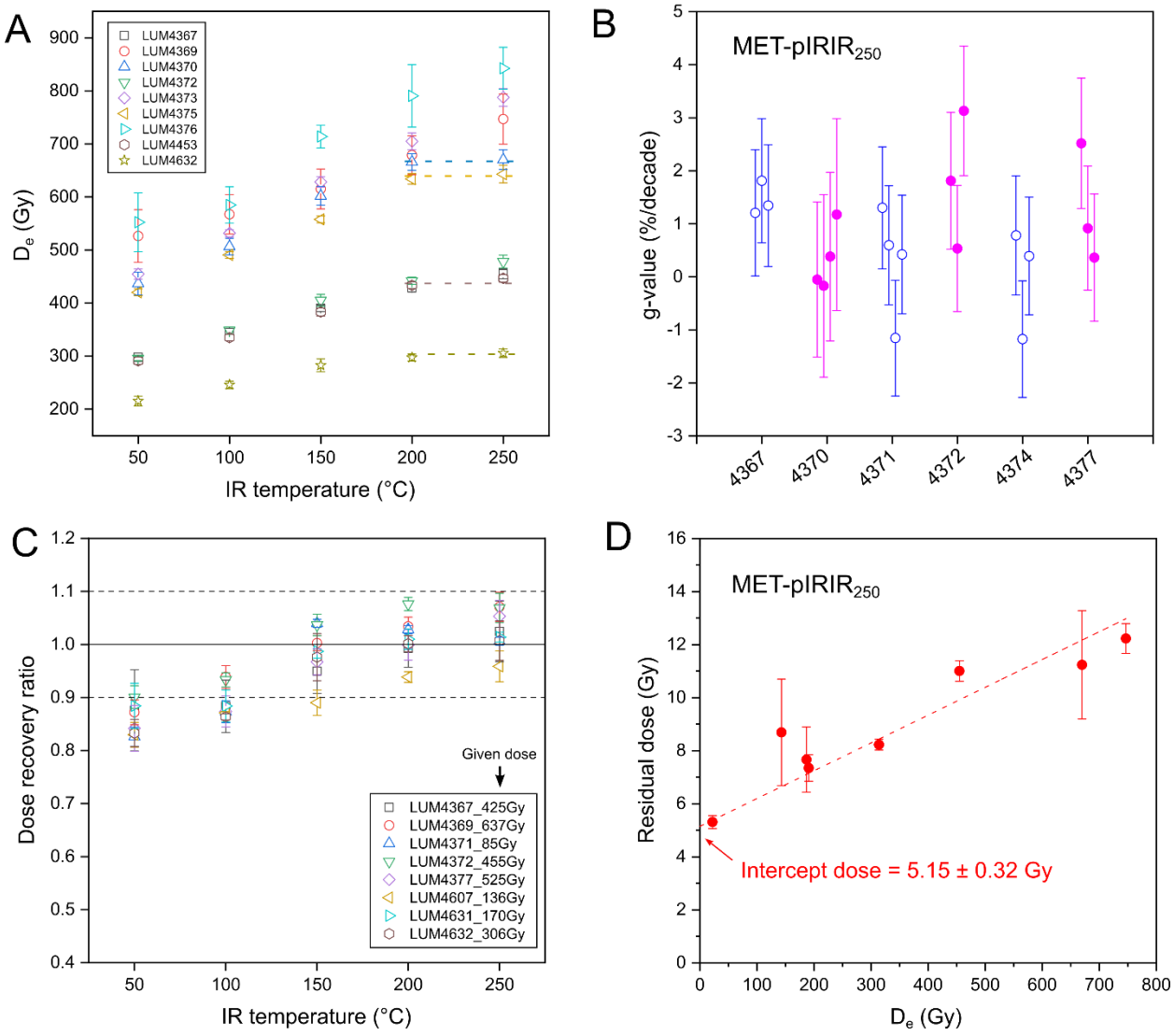

Fig. 6. A) Fine-grained polymineral D_e values at different IR stimulation temperatures with the MET-pIRIR$_{250}$ protocol. Each data point is an average of 6-10 aliquots. B) Fading rates (g-values) of 5 samples. Each data point is one aliquot. C) Dose recovery ratios at different IR stimulation temperatures. Each data point is an average of 3-4 aliquots. D) Residual doses versus D_e values for the MET-pIRIR250 signal. Each data point is an average of 3 aliquots. An intercept dose of 5.2 Gy is obtained with a linear fitting.

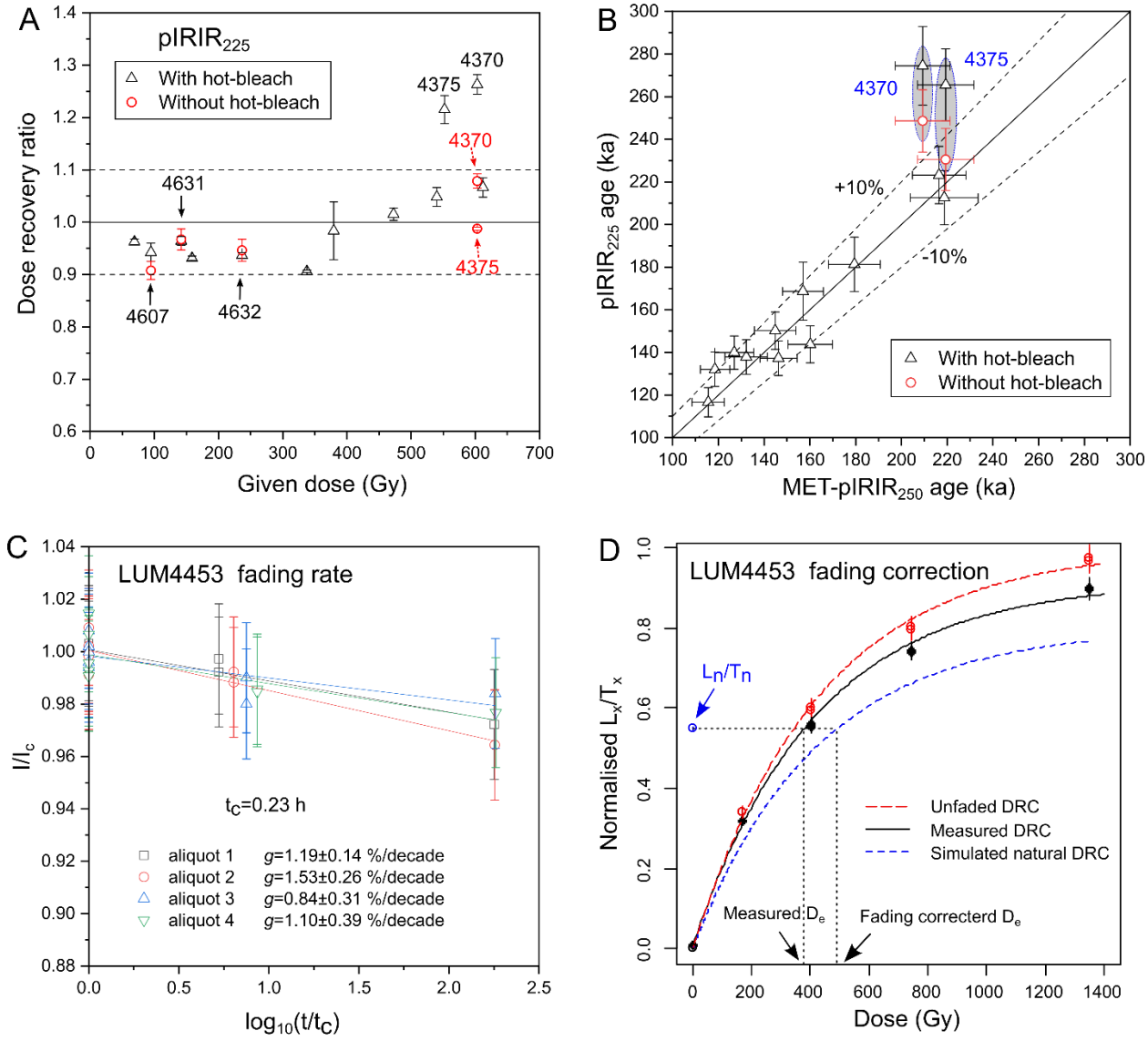

Fig. 7. A) Dose recovery ratios of the $pIRIR_{225}$ signal for fine-grained polymineral, with and without hot-bleach at the end of each cycle. B) Comparison of fading corrected $pIRIR_{225}$ ages and uncorrected MET-$pIRIR_{250}$ ages. C) Fading rate measurements of the $pIRIR_{225}$ signal of sample LUM4453. D) Fading correction of the $pIRIR_{225}$ signal for sample LUM4453.

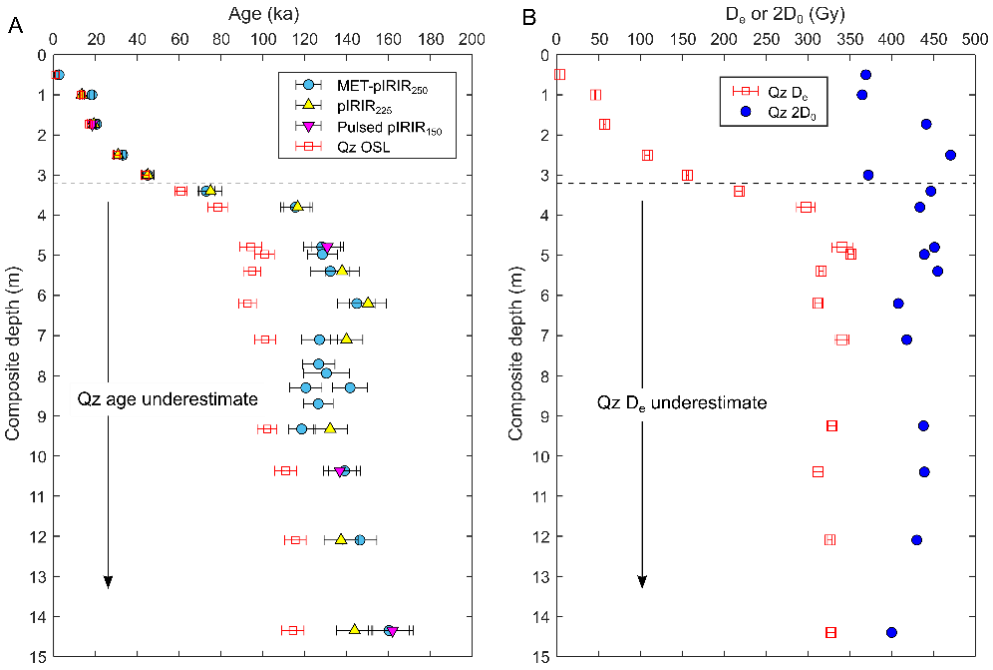

Fig. 8. A) Quartz OSL ages and polymineral pIRIR ages plotted against composite depth. Quartz OSL ages start to underestimate pIRIR ages when the sample is older than 50 ka. B) Quartz D_e starts to be underestimated when the D_e is >156 Gy. However, the $2D_0$ values (empirical dating limit) are around 400 Gy.

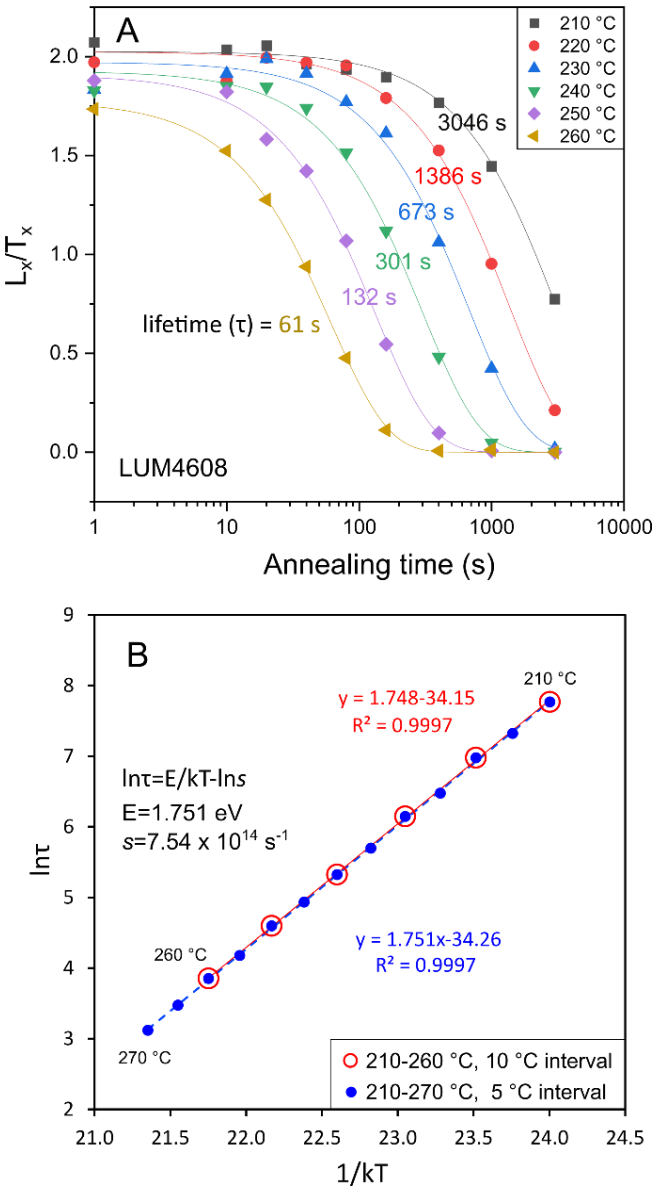

Fig. 9. A) Isothermal annealing at different temperatures for the quartz OSL signal of sample LUM4608. B) Linear fitting to estimate the electron trap depth (E) and frequency factor (*s*). Note that the parameters derived from six annealing temperatures are similar to those obtained from thirteen annealing temperatures.

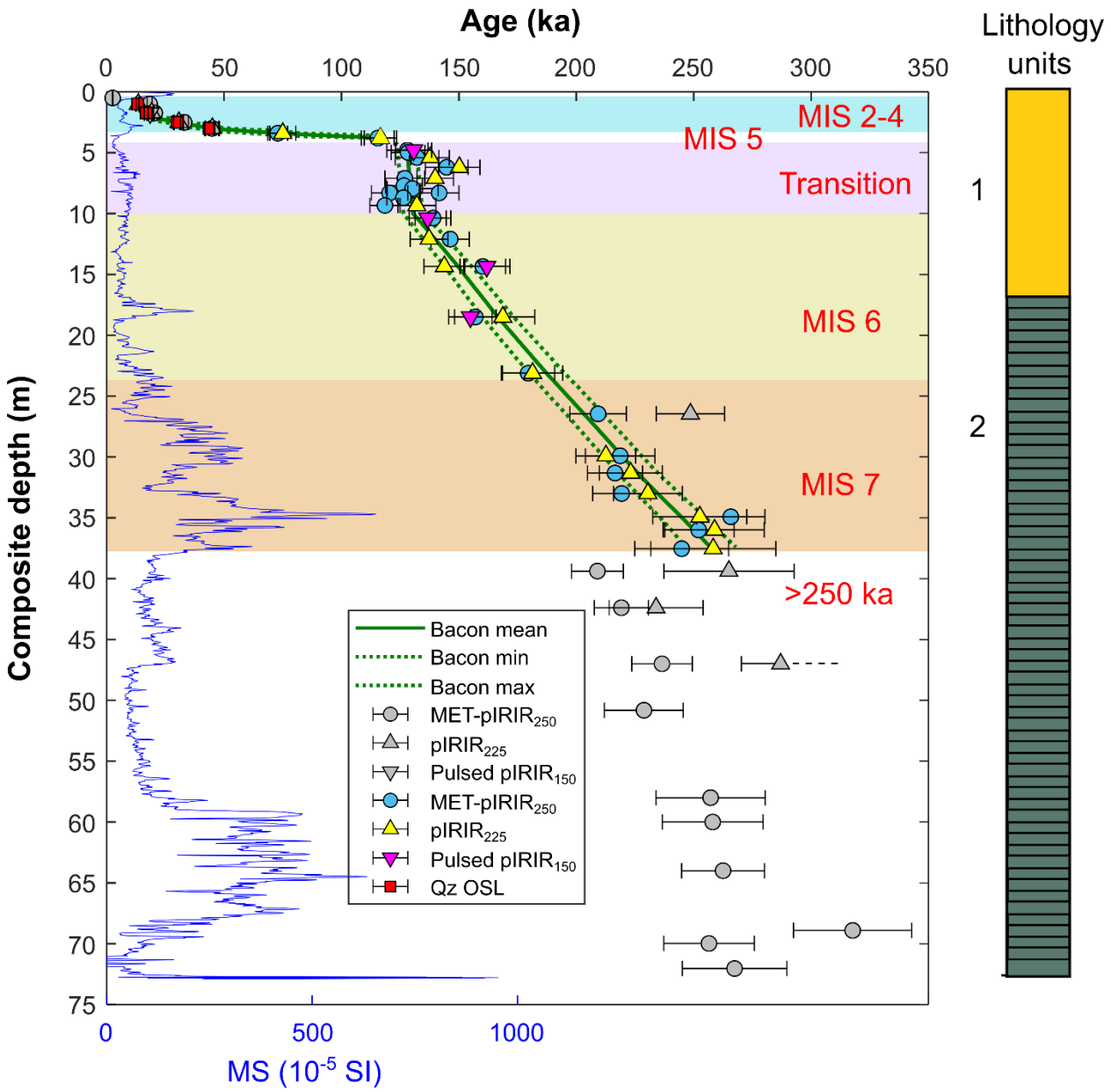

Fig. 10. Bacon age-depth model with lithology for ROD11. Colored symbols are used for modelling, while grey symbols are not used for modelling. Lithologic unit 1 is loess, and unit 2 is laminated or layered sediments, i.e. lacustrine sediments and loess derivates.

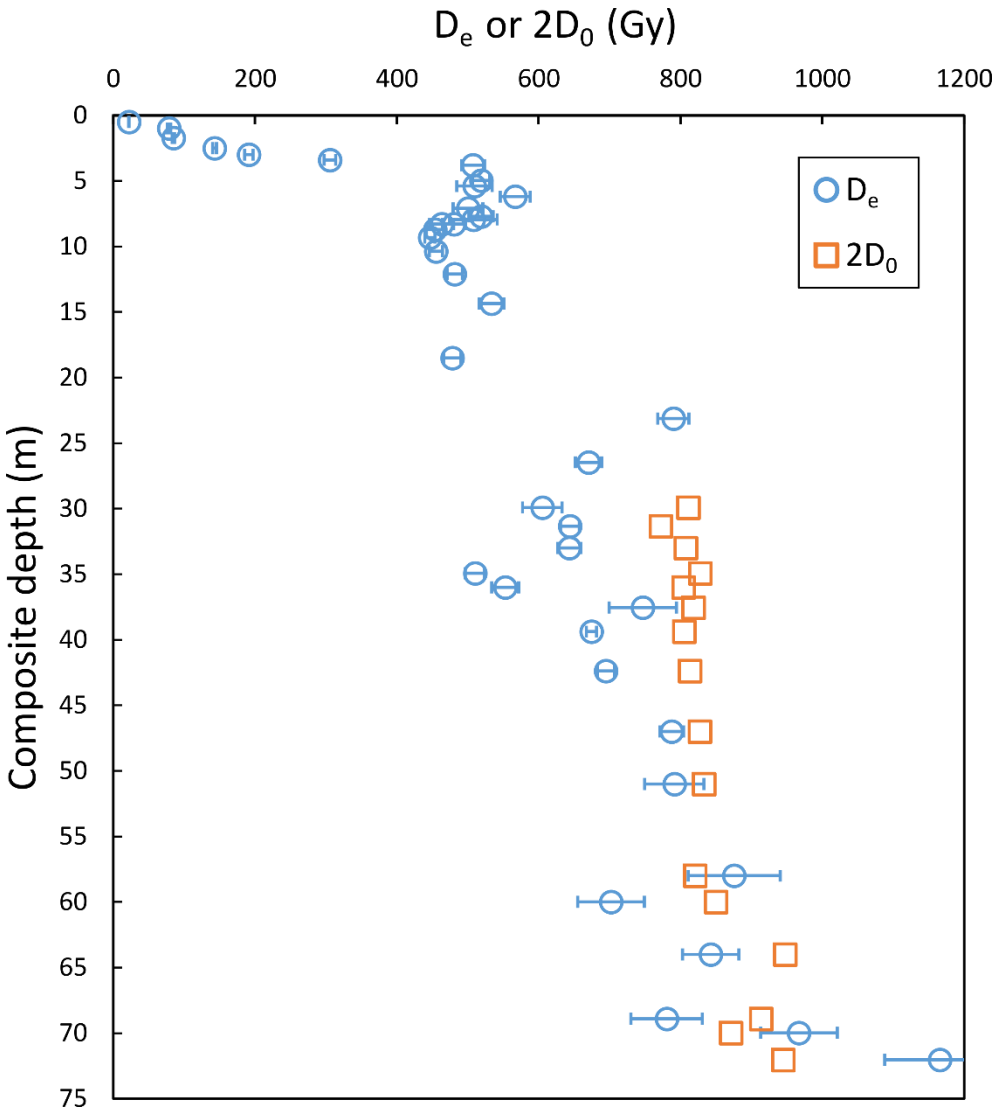

Fig. 11. D_e vs $2D_0$ for the MET-pIRIR$_{250}$ signal. The $2D_0$ is around 800 Gy. D_e values start to be underestimated when they are close to 800 Gy.

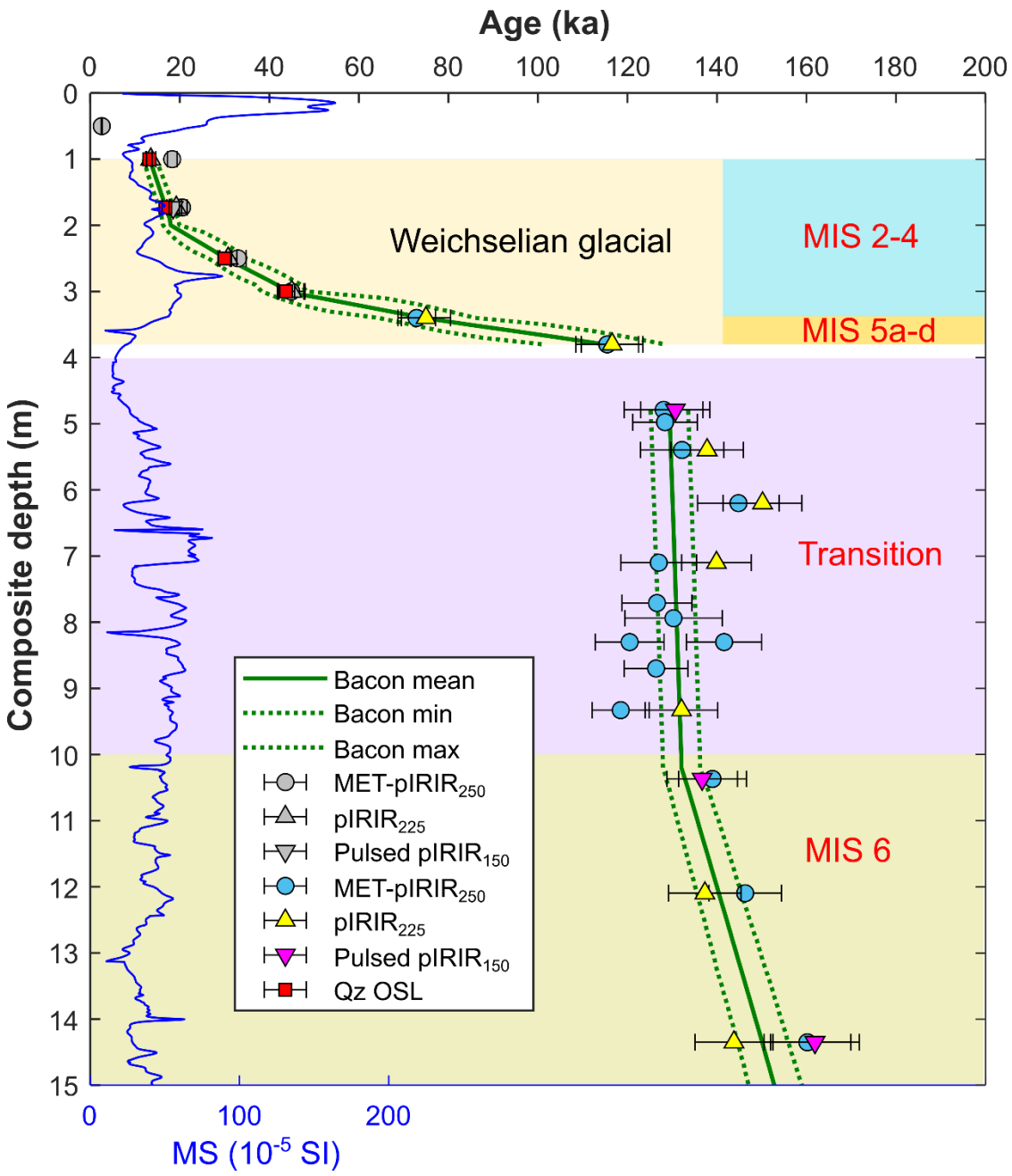

Fig. 12. Bacon age-depth model and subdivision of the age framework for the upper 15 m of sediments for ROD11. Note that the Eemian soil is missing from the records at Rodderberg.

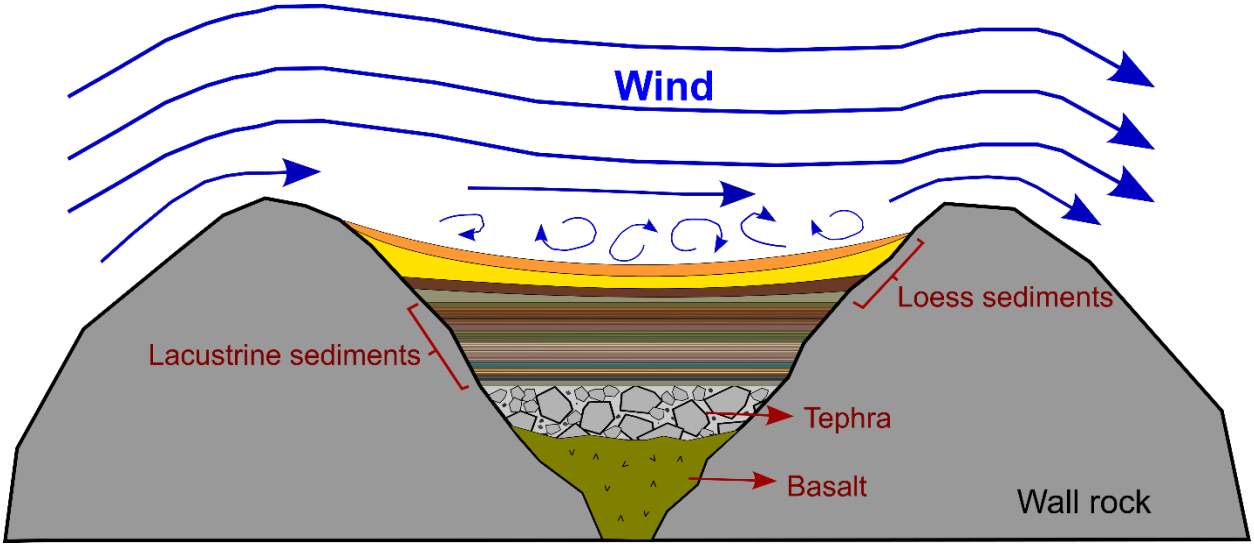

Fig. 13. Wind erosion at the Rodderberg crater basin. The wind turbulence blew out the Eemian soil during the Late Eemian Aridity Pulse (LEAP) at ca. 118 ka, and multiple erosional events happened during the following Weichselian glacial.

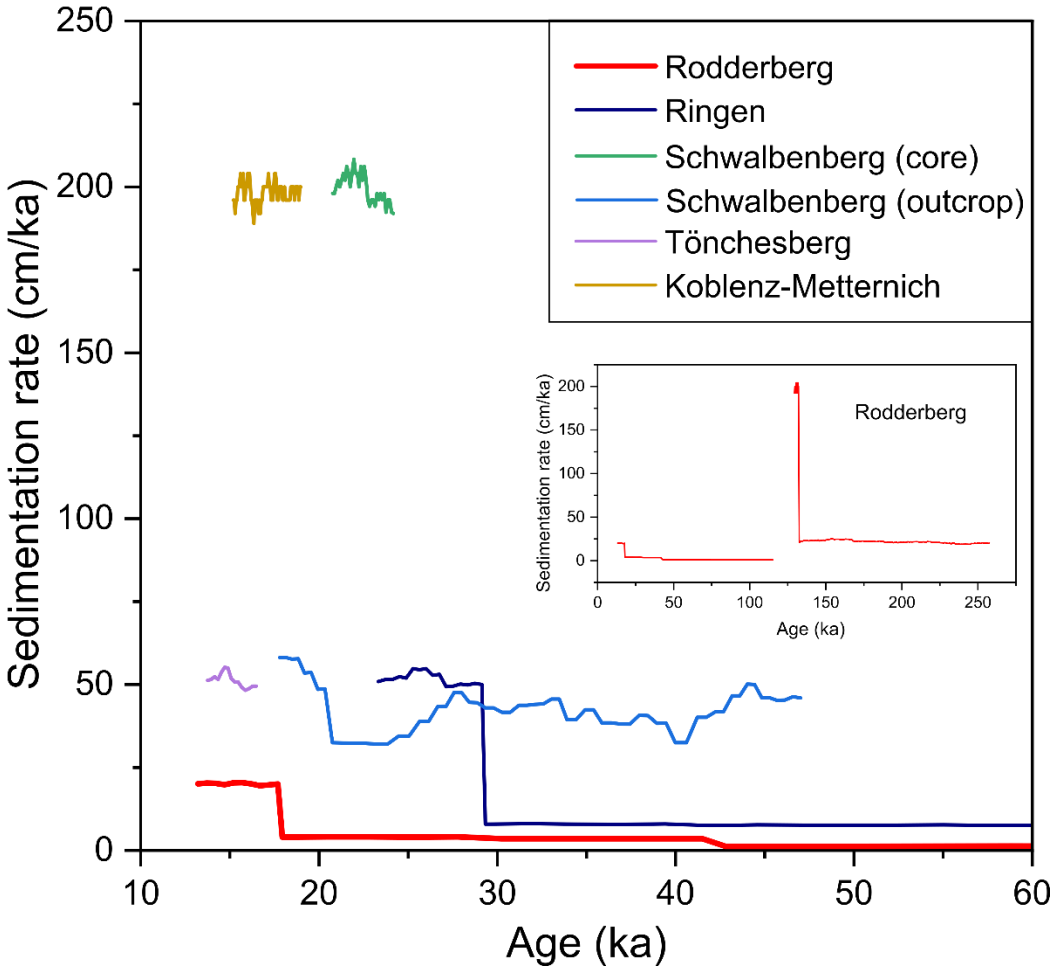

Fig. 14. Sedimentation rates of Rodderberg and other nearby loess sections in the Middle Rhine Valley during the last glacial period. The inset graph shows the sedimentation rate of Rodderberg above 37.5 m depth in the core. For the other loess sections, we adopted the luminescence ages from previous studies and performed Bacon age-depth modelling. Quartz OSL ages are used for Ringen (Zens et al., 2018) and the sediment core from Schwalbenberg (Klasen et al., 2015). Fading uncorrected IRSL ages are used for the Schwalbenberg outcrop (Frechen and Schirmer, 2011) and Koblenz-Metternich (Frechen et al., 2003) and fading uncorrected TL ages are used for Tönchesberg (Frechen et al., 2003), which means that the ages of these three loess sections are ca. 20% underestimated. Note that the sedimentation rate at Rodderberg is the lowest indicating erosional events.